

THE REST-FRAME OPTICAL LUMINOSITY FUNCTIONS OF GALAXIES AT $2 \leq z \leq 3.5$ ¹

D. MARCHESINI², P. VAN DOKKUM², R. QUADRI², G. RUDNICK³, M. FRANX⁴, P. LIRA⁵, S. WUYTS⁴, E. GAWISER^{2,5,6},
D. CHRISTLEIN^{2,5}, S. TOFT^{2,7}

Accepted for publication in the Astrophysical Journal

ABSTRACT

We present the rest-frame optical (B , V , and R band) luminosity functions (LFs) of galaxies at $2 \leq z \leq 3.5$, measured from a K -selected sample constructed from the deep NIR MUSYC, the ultra-deep FIRES, and the GOODS-CDFS. This sample is unique for its combination of area and range of luminosities. The faint-end slopes of the LFs at $z > 2$ are consistent with those at $z \sim 0$. The characteristic magnitudes are significantly brighter than the local values (e.g., ~ 1.2 mag in the R band), while the measured values for Φ^* are typically ~ 5 times smaller. The B -band luminosity density at $z \sim 2.3$ is similar to the local value, and in the R band it is ~ 2 times smaller than the local value. We present the LF of Distant Red Galaxies (DRGs), which we compare to that of non-DRGs. While DRGs and non-DRGs are characterized by similar LFs at the bright end, the faint-end slope of the non-DRG LF is much steeper than that of DRGs. The contribution of DRGs to the global densities down to the faintest probed luminosities is 14%-25% in number and 22%-33% in luminosity. From the derived rest-frame $U-V$ colors and stellar population synthesis models, we estimate the mass-to-light ratios (M/L) of the different subsamples. The M/L ratios of DRGs are ~ 5 times higher (in the R and V bands) than those of non-DRGs. The global stellar mass density at $2 \leq z \leq 3.5$ appears to be dominated by DRGs, whose contribution is of order $\sim 60\%$ - 80% of the global value. Qualitatively similar results are obtained when the population is split by rest-frame $U-V$ color instead of observed $J-K$ color.

Subject headings: galaxies: distances and redshifts — galaxies: evolution — galaxies: formation — galaxies: fundamental parameters — galaxies: high-redshift — galaxies: luminosity function, mass function — galaxies: stellar content — infrared: galaxies

1. INTRODUCTION

Understanding the formation mechanisms and evolution with cosmic time of galaxies is one of the major goals of observational cosmology. In the current picture of structure formation, dark matter halos build up in a hierarchical fashion controlled by the nature of the dark matter, the power spectrum of density fluctuations, and the parameters of the cosmological model. The assembly of the stellar content of galaxies is governed by much more complicated physics, such as the mechanisms of star formation, gaseous dissipation, the feedback of stellar and central supermassive black hole energetic output on the baryonic material of the galaxies, and mergers.

The mean space density of galaxies per unit luminosity, or luminosity function (LF), is one of the most fundamental of all cosmological observables, and it is one of the most basic descriptors of a galaxy population. The shape of the LF retains the imprint of galaxy formation and evolution processes; the evolution of the LF as a function of cosmic time, galaxy type and environment provides insights into the physical processes that govern the assembly and the following evolution of galaxies. Therefore, the LF represents one of the funda-

mental observational tools to constrain the free parameters of theoretical models.

The local ($z \sim 0$) LF has been very well determined from several wide-area, multi-wave band surveys with follow-up spectroscopy (Norberg et al. 2002; Blanton et al. 2001, 2003; Kochanek et al. 2001; Cole et al. 2001). At intermediate redshifts ($z \sim 0.75$), spectroscopic surveys found a steepening of the faint-end LF with increasing redshift in the global LF, mainly due to the contribution by later type galaxies (Lilly et al. 1995; Ellis et al. 1996). From the COMBO-17 survey, Wolf et al. (2003) measured the rest-frame optical LF up to $z \sim 1.2$, finding that early-type galaxies show a decrease of a factor of ~ 10 in the characteristic density Φ^* of the LF. The latest type galaxies show a brightening of ~ 1 mag in M^* (the characteristic magnitude) and an increase of ~ 1.6 in Φ^* in their highest redshift bin in the blue band. Further progress in the measurement of the LF at $z < 2$ was obtained with the VIMOS VLT Deep Survey (VVDS; Le Fèvre et al. 2004) and the DEEP-2 Galaxy Redshift Survey (Davis et al. 2003). From the VVDS data, Ilbert et al. (2005) measured the rest-frame optical LF from $z = 0.05$ to $z = 2$. From the same data set, Zucca et al. (2006) performed a similar analysis for different spectral galaxy types, finding a significant steepening of the LF going from early to late types. Their results indicate a strong type-dependent evolution of the LF, and identify the latest spectral types as responsible for most of the evolution of the UV-optical LF out to $z = 1.5$.

Contrary to low-redshift studies, the selection of high-redshift ($z > 2$) galaxies still largely relies on their colors. One of the most efficient ways to select high-redshift galaxies is the Lyman drop-out technique, which enabled Steidel and collaborators to build large samples of $z \sim 3$ star-forming galaxies (Steidel et al. 1996, 1999). Extensive studies of these optically (rest-frame ultraviolet) selected galaxies at $z \sim 3$

¹ Based on observations with the NASA/ESA *Hubble Space Telescope*, obtained at the Space Telescope Science Institute, which is operated by AURA, Inc., under NASA contract NAS5-26555. Also based on observations collected at the European Southern Observatories on Paranal, Chile as part of the ESO program 164.O-0612.

² Department of Astronomy, Yale University, New Haven, CT
Electronic address: danilom@astro.yale.edu

³ Goldberg Fellow, National Optical Astronomical Observatory, Tucson, AZ

⁴ Leiden Observatory, Leiden University, Leiden, Netherlands

⁵ Departamento de Astronomía, Universidad de Chile, Santiago, Chile

⁶ National Science Foundation Astronomy and Astrophysics Postdoctoral Fellow

⁷ European Southern Observatory, Garching bei München, Germany

(Lyman Break Galaxies [LBGs]) and at $z \sim 2$ (BM/BX galaxies; Steidel et al. 2004; Adelberger et al. 2004) have shown that they are typically characterized by low extinction, modest ages, stellar masses $\sim 10^{10} M_{\odot}$, and star formation rates of $10\text{--}100 M_{\odot}\text{yr}^{-1}$ (Steidel et al. 2003; Shapley et al. 2001; Reddy et al. 2005). Shapley et al. (2001) recovered the rest-frame V -band LF of LBGs at $z \sim 3$ from the rest-frame UV LF (Steidel et al. 1999; but see also Sawicki & Thompson 2006), finding that the LBG LF is characterized by a very steep faint end.

LBGs dominate the UV luminosity density at $z \sim 2\text{--}6$, as well as possibly the global star formation rate density at these redshifts (Reddy et al. 2005). However, since the Lyman break selection technique requires galaxies to be very bright in the rest-frame UV in order to be selected, it might miss galaxies that are heavily obscured by dust or whose light is dominated by evolved stellar populations. These objects can be selected in the near-infrared (NIR), which corresponds to the rest-frame optical out to $z \sim 3$. Using the NIR selection criterion $J - K > 2.3$ (also suggested by Saracco et al. 2001), Franx et al. (2003) and van Dokkum et al. (2003) discovered a new population of high-redshift galaxies (distant red galaxies [DRGs]) that would be largely missed by optically selected surveys. Follow-up studies have shown that DRGs constitute a heterogeneous population. They are mostly actively forming stars at $z \sim 1.5\text{--}3.5$ (van Dokkum et al. 2003; Förster Schreiber et al. 2004; Rubin et al. 2004; Knudsen et al. 2005; Reddy et al. 2005; Papovich et al. 2006). However, some show no signs of active star formation and appear to be passively evolving (Labbé et al. 2005; Kriek et al. 2006; Reddy et al. 2006), while others seem to host powerful active galactic nuclei (van Dokkum et al. 2004; Papovich et al. 2006). Compared to LBGs, DRGs have systematically older ages and larger masses (Förster Schreiber et al. 2004), although some overlap between the two exists (Shapley et al. 2005; Reddy et al. 2005). Recently, van Dokkum et al. (2006) have demonstrated that in a mass-selected sample ($> 10^{11} M_{\odot}$) at $2 < z < 3$, DRGs make up 77% in mass, compared to only 17% from LBGs (see also Papovich et al. 2006), implying that the rest-frame optical LF determined by Shapley et al. (2001) is incomplete.

The global (i.e., including all galaxy types) rest-frame optical LF at $z > 2$ can be studied by combining multiwavelength catalogs with photometric redshift information. Giallongo et al. (2005) studied the B -band LFs of red and blue galaxies. They find that the B -band number densities of red and blue galaxies have different evolution, with a strong decrease of the red population at $z = 2\text{--}3$ compared to $z = 0$ and a corresponding increase of the blue population, in broad agreement with the predictions from their hierarchical cold dark matter models. As all previous works at $z > 2$ are based on either very deep photometry but small total survey area (Poli et al. 2003; Giallongo et al. 2005) or larger but still single field surveys (Gabasch et al. 2004), their results are strongly affected by field-to-field variations and by low number statistics, especially at the bright end. Moreover, Gabasch et al. (2004) used an I -band-selected data set from the FORS Deep Field. The I band corresponds to the rest-frame UV at $z \sim 2$, which means that significant extrapolation is required.

In this paper we take advantage of the deep NIR MUSYC survey to measure the rest-frame optical (B , V , and R band) LFs of galaxies at $2 \leq z \leq 3.5$. Its unique combination of surveyed area and depth allows us to (1) minimize the effects of field-to-field variations, (2) better probe the bright end of

the LF with good statistics, and (3) sample the LF down to luminosities ~ 0.9 mag fainter than the characteristic magnitude. To constrain the faint-end slope of the LF and to increase the statistics, we also made use of the FIRES and the GOODS-CDFS surveys, by constructing a composite sample. The large number of galaxies in our composite sample also allows us to measure the LFs of several subsamples of galaxies, such as DRGs and non-DRGs (defined based on their observed $J - K$ color), and of intrinsically red and blue galaxies (defined based on their rest-frame $U - V$ color).

This paper is structured as follows. In § 2 we present the composite sample used to measure the LF of galaxies at $2 \leq z \leq 3.5$; in § 3 we describe the methods applied to measure the LF and discuss the uncertainties in the measured LF due to field-to-field variations and errors in the photometric redshift estimates; the results (of all galaxies and of the individual subsamples considered in this work) are presented in § 4, while the estimates of the number and luminosity densities and the contribution of DRGs (red galaxies) to the global stellar mass density are given in § 5. Our results are summarized in § 6. We assume $\Omega_M = 0.3$, $\Omega_{\Lambda} = 0.7$, and $H_0 = 70 \text{ km s}^{-1} \text{ Mpc}^{-1}$ throughout the paper. All magnitudes and colors are on the Vega system, unless identified as “AB”. Throughout the paper, the $J - K$ color is in the observed frame, while the $U - V$ color refers to the rest frame.

2. THE COMPOSITE SAMPLE

The data set we have used to estimate the LF consists of a composite sample of galaxies built from three deep multiwavelength surveys, all having high-quality optical to NIR photometry: the “ultradeep” Faint InfraRed Extragalactic Survey (FIRES; Franx et al. 2003), the Great Observatories Origins Deep Survey (GOODS; Giavalisco et al. 2004; Chandra Deep Field–South [CDF-S]), and the Multi-wavelength Survey by Yale–Chile (MUSYC; Gawiser et al. 2006; Quadri et al. 2007b). Photometric catalogs were created for all fields in the same way, following the procedures of Labbé et al. (2003).

FIRES consists of two fields, namely, the Hubble Deep Field–South proper (HDF-S) and the field around MS 1054–03, a foreground cluster at $z = 0.83$. A complete description of the FIRES observations, reduction procedures, and the construction of photometric catalogs is presented in detail in Labbé et al. (2003) and Förster Schreiber et al. (2006) for HDF-S and MS 1054–03, respectively. Briefly, the FIRES HDF-S and MS 1054–03 (hereafter FH and FMS, respectively) are K_s band-limited multicolor source catalogs down to $K_s^{\text{tot}} = 24.14$ and $K_s^{\text{tot}} = 23.14$, for a total of 833 and 1858 sources over fields of $2.5' \times 2.5'$ and $5.5' \times 5.3'$, respectively. The FH and FMS catalogs have 90% completeness level at $K_s^{\text{tot}} = 23.8$ and $K_s^{\text{tot}} = 22.85$, respectively. The final FH (FMS) catalogs used in the construction of the composite sample has 358 (1427) objects over an effective area of 4.74 (21.2) arcmin², with $K_s^{\text{tot}} < 23.14$ (22.54), which for point sources corresponds to a 10 (8) σ signal-to-noise ratio (S/N) in the custom isophotal aperture.

From the GOODS/EIS observations of the CDF-S (data release version 1.0) a K_s band limited multicolor source catalog (hereafter CDFS) was constructed, described in S. Wuyts et al. (2007, in preparation). GOODS zero points were adopted for J and K_s . The H -band zero point was obtained by matching the stellar locus on a $J - K$ versus $J - H$ color-color diagram to the stellar locus in FIRES HDF-S and MS 1054–03. The difference with the official GOODS H -band zero point varies across the field, but on average our H -band zero points are

TABLE 1
THE COMPOSITE SAMPLE: FIELD SPECIFICATIONS

Field	Filter Coverage	K_{90}^{tot} (mag)	$K_{\text{lim,cs}}^{\text{tot}}$ (mag)	Area (arcmin ²)	N	N_{spec}
FIRES-HDFS	U ₃₀₀ B ₄₅₀ V ₆₀₆ I ₈₁₄ J _s HK _s	23.80	23.14	4.74	358	68
FIRES-MS1054	UBVV ₆₀₆ I ₈₁₄ J _s HK _s	22.85	22.54	21.2	1427	297
GOODS-CDFS	B ₄₃₅ V ₆₀₆ i ₇₇₅ Z ₈₅₀ JHK _s	21.94	21.34	65.6	1588	215
MUSYC	UBVRIZJHK _s	21.33	21.09	286.1	5507	116

NOTE. — K_{90}^{tot} is the K_s band total magnitude 90% completeness limit, $K_{\text{lim,cs}}^{\text{tot}}$ is the K_s band total magnitude limit used to construct the composite sample, N is the total number of sources down to $K_{\text{lim,cs}}^{\text{tot}}$, and N_{spec} is the number of objects with spectroscopic redshift.

~ 0.1 mag brighter. A total effective area of 65.6 arcmin² is well exposed in all bands. The final catalog contains 1588 objects with $K_s^{\text{tot}} < 21.34$ in this area. At $K_s^{\text{tot}} = 21.34$ the median S/N in the K_s isophotal aperture is ~ 12 .

MUSYC consists of optical and NIR imaging of four independent $30' \times 30'$ fields with extensive spectroscopic follow-up (Gawiser et al. 2006). Deeper NIR JHK_s imaging was obtained over four $10' \times 10'$ subfields with the ISPI camera at the Cerro Tololo Inter-American Observatory (CTIO) Blanco 4 m telescope. A complete description of the deep NIR MUSYC observations, reduction procedures, and the construction of photometric catalogs will be presented in Quadri et al. (2007b). The 5σ point-source limiting depths are $J \sim 22.9$, $H \sim 21.8$, and $K_s \sim 21.3$. The optical $UBVRIZ$ data are described in Gawiser et al. (2006). The present work is restricted to three of the four deep fields: the two adjacent fields centered around HDF-S proper (hereafter MH1 and MH2) and the field centered around the quasar SDSS 1030+05 (M1030). The final MUSYC K_s -selected catalog used in the construction of the composite sample has 5507 objects over an effective area of 286.1 arcmin², with $K_s^{\text{tot}} < 21.09$, which for point sources corresponds to a $\sim 10\sigma S/N$ in the isophotal aperture.

Table 1 summarizes the specifications of each field, including wave band coverage, K_s band total magnitude 90% completeness limit (K_{90}^{tot}), effective area, the K_s band total magnitude limit used to construct the composite sample ($K_{\text{lim,cs}}^{\text{tot}}$), the number of objects, and the number of sources with spectroscopic redshifts.

Only a few percent of the sources in the considered catalogs have spectroscopic redshift measurements. Consequently, we must rely primarily on photometric redshift estimates. Photometric redshifts z_{phot} for all galaxies are derived using an identical code to that presented in Rudnick et al. (2001, 2003), but with a slightly modified template set. This code models the observed spectral energy distribution (SED) using nonnegative linear combinations of a set of eight galaxy templates. As in Rudnick et al. (2003), we use the E, Sbc, Scd, and Im SEDs from Coleman et al. (1980), the two least reddened starburst templates from Kinney et al. (1996), and a synthetic template corresponding to a 10 Myr old simple stellar population (SSP) with a Salpeter (1955) stellar initial mass function (IMF). We also added a 1 Gyr old SSP with a Salpeter IMF, generated with the Bruzual & Charlot (2003) evolutionary synthesis code. The empirical templates have been extended into the UV and the NIR using models. Comparing the photometric redshifts with 696 spectroscopic redshifts (63 at $z \geq 1.5$) collected from the literature and from our own observations gives a scatter in $\Delta z/(1+z)$ of $\sigma = 0.06$. Restricting the analysis to galaxies at $z \geq 1.5$ in the MUSYC fields gives $\sigma = 0.12$, corresponding to $\Delta z \approx 0.4$ at $z = 2.5$. Approximately 5% of

galaxies in this sample are ‘‘catastrophic’’ outliers. A full discussion of the quality of the photometric redshifts is given elsewhere (Quadri et al. 2007b). The effects of photometric redshift errors on the derived LFs are modeled in § 3.3.

Rest-frame luminosities are computed from the observed SEDs and redshift information using the method extensively described in the Appendix of Rudnick et al. (2003). This method does not depend directly on template fits to the data but rather interpolates directly between the observed fluxes, using the best-fit templates as a guide. We computed rest-frame luminosities in the U , B , V , and R filters of Bessell (1990). For these filters we use $M_{\odot,U} = +5.66$, $M_{\odot,B} = +5.47$, $M_{\odot,V} = +4.82$, and $M_{\odot,R} = +4.28$. In all cases where a spectroscopic redshift is available we computed the rest-frame luminosities fixed at z_{spec} .

Stars in all K_s -selected catalogs were identified by spectroscopy, by fitting the object SEDs with stellar templates from Hauschildt et al. (1999) and/or inspecting their morphologies, as in Rudnick et al. (2003). On average, approximately 10% of all the objects were classified as stars.

We constructed a composite sample of high-redshift ($2 \leq z \leq 3.5$) galaxies to be used in the estimate of the LF in § 3. A large composite sample with a wide range of luminosities is required to sample both the faint and the bright end of the LF well; moreover, a large surveyed area is necessary to account for sample variance. The very deep FIRES allows us to constrain the faint end of the LF, while the large area of MUSYC allows us to sample the bright end of the LF very well. The CDFS catalog bridges the two slightly overlapping regimes and improves the number statistics. The final composite sample includes 442, 405, and 547 K_s -selected galaxies in the three targeted redshift intervals $2 \leq z \leq 2.5$, $2.7 \leq z \leq 3.3$, and $2.5 < z \leq 3.5$, respectively, for a total of 989 galaxies with $K_s^{\text{tot}} < 23.14$ at $2 \leq z \leq 3.5$. Of these, $\sim 4\%$ have spectroscopic redshifts. In Figure 1 we show the rest-frame B -band absolute magnitude versus the redshift for the composite sample in the studied redshift range $2 \leq z \leq 3.5$.

3. METHODOLOGY

3.1. The $1/V_{\text{max}}$ Method

To estimate the observed LF in the case of a composite sample, we have applied an extended version of the $1/V_{\text{max}}$ algorithm (Schmidt 1968) as defined in Avni & Bahcall (1980) so that several samples can be combined in one calculation. For a given redshift interval $[z_1, z_2]$, we computed the galaxy number density $\Phi(M)$ in each magnitude bin ΔM in the following way:

$$\Phi(M) = \frac{1}{\Delta M} \sum_{i=1}^N \frac{1}{V_i}, \quad (1)$$

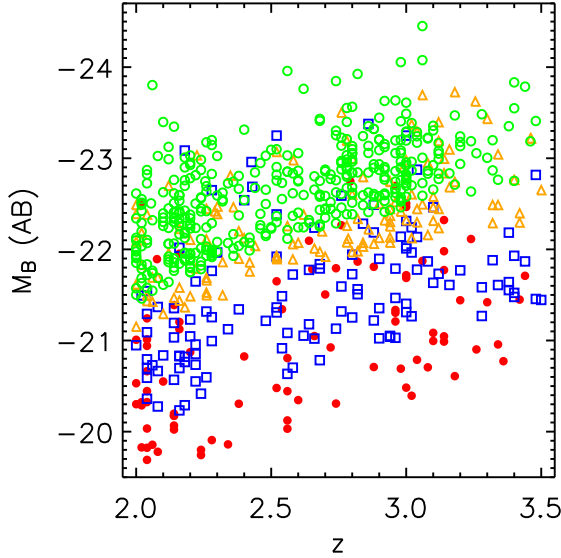


FIG. 1.— Rest-frame B -band magnitude vs. redshift for the composite sample in the redshift range $2 \leq z \leq 3.5$; the FH, FMS, CDFS, and MUSYC fields are plotted as red filled circles, blue open squares, orange open triangles, and green open circles, respectively.

where N is the number of objects in the chosen bin and V_i is:

$$V_i = \sum_{j=1}^n \omega_j \int_{z_{\min}}^{z_{\text{up}}(i,j)} \frac{dV}{dz} dz, \quad (2)$$

where ω_j is the area in units of steradians corresponding to the j th field, n is the number of samples combined together, dV/dz is the comoving volume element per steradian, and $z_{\text{up}}(i, j)$ is the minimum of z_2 and the maximum redshift at which the i th object could have been observed within the magnitude limit of the j th sample. The Poisson error in each magnitude bin was computed adopting the recipe of Gehrels (1986) valid also for small numbers.

The $1/V_{\max}$ estimator has the advantages of simplicity and no a priori assumption of a functional form for the luminosity distribution; it also yields a fully normalized solution. However, it can be affected by the presence of clustering in the sample, leading to a poor estimate of the faint-end slope of the LF. Although field-to-field variation represents a significant source of uncertainty in deep surveys (since they are characterized by very small areas and hence small sampled volumes), the majority of published cosmological number densities and related quantities do not properly account for sample variance in their quoted error budgets. Our composite sample is made of several independent fields with a large total effective area of ~ 380 arcmin² (about a factor of 3 larger than the nominal area of the K_s -selected CDFS-GOODS catalog used in Dahlen et al. 2005), which significantly reduces the uncertainties due to sample variance. Also, the large number of fields considered in this work with their large individual areas allows us to empirically measure the field-to-field variations from one field to the other in the estimate of the LF with the $1/V_{\max}$ method, especially at the bright end, and to properly account for it in the error budget.

In order to quantify the uncertainties due to field-to-field variations in the determination of the LF, we proceeded as follows. First, for each magnitude bin ΔM , we measured Φ^j for each individual j th field using equation (1). For each magnitude bin with $n \geq 3$, we estimated the contribution to the error

budget of $\Phi(M)$ from sample variance using:

$$\sigma_{\text{sv}} = \frac{\text{rms}(\Phi^j)}{\sqrt{n}}, \quad (3)$$

with n the number of individual fields used. For the magnitude bins with $n \leq 2$ (usually the brightest bin and the 3-4 faintest ones), we adopted the mean of the $\text{rms}(\Phi^j)$ with $n \geq 3$. The final 1σ error associated to $\Phi(M)$ is then $\sigma = (\sigma_{\text{Poi}}^2 + \sigma_{\text{sv}}^2)^{1/2}$, with σ_{Poi} the Poisson error in each magnitude bin.

3.2. The Maximum Likelihood Method

We also measured the observed LF using the STY method (Sandage et al. 1979), which is a parametric maximum likelihood estimator. The STY method has been shown to be unbiased with respect to density inhomogeneities (e.g., Efstathiou et al. 1988), it has well-defined asymptotic error properties (e.g. Kendall & Stuart 1961), and does not require binning of the data. The STY method assumes that $\Phi(M)$ has a universal form, i.e., the number density of galaxies is separable into a function of luminosity times a function of position: $n(M, \mathbf{x}) = \Phi(M)\rho(\mathbf{x})$. Therefore, the shape of $\Phi(M)$ is determined independently of its normalization. We have assumed that $\Phi(M)$ is described by a Schechter (1976) function,

$$\Phi(M) = (0.4 \ln 10) \Phi^* \left[10^{0.4(M^* - M)(1 + \alpha)} \right] \times \exp \left[-10^{0.4(M^* - M)} \right], \quad (4)$$

where α is the faint-end slope parameter, M^* is the characteristic absolute magnitude at which the LF exhibits a rapid change in the slope, and Φ^* is the normalization.

The probability of seeing a galaxy of absolute magnitude M_i at redshift z_i in a magnitude-limited catalog is given by

$$p_i \propto \frac{\Phi(M_i)}{\int_{M_{\text{faint}}(z_i)}^{M_{\text{bright}}(z_i)} \Phi(M) dM}, \quad (5)$$

where $M_{\text{faint}}(z_i)$ and $M_{\text{bright}}(z_i)$ are the faintest and brightest absolute magnitudes observable at the redshift z_i in a magnitude-limited sample. The likelihood $\Lambda = \prod_{i=1}^N p_i$ (where the product extends over all galaxies in the sample) is maximized with respect to the parameters α and M^* describing the LF $\Phi(M)$. The best-fit solution is obtained by minimizing $-2 \ln \Lambda$. A simple and accurate method of estimating errors is to determine the ellipsoid of parameter values defined by

$$\ln \Lambda = \ln \Lambda_{\max} - \frac{1}{2} \chi_{\beta}^2(S), \quad (6)$$

where $\chi_{\beta}^2(S)$ is the β -point of the χ^2 distribution with S degrees of freedom. Parameter $\chi_{\beta}^2(S)$ is chosen in the standard way depending on the desired confidence level in the estimate (as described, e.g., by Avni 1976; Lampton et al. 1976): $\chi_{\beta}^2(2) = 2.3, 6.2,$ and 11.8 to estimate $\alpha - M^*$ error contours with 68%, 95%, and 99% confidence level (1, 2, and 3 σ , respectively). The value of Φ^* is then obtained by imposing a normalization on the best-fit LF such that the total number of observed galaxies in the composite sample is reproduced. The 1, 2, and 3 σ errors on Φ^* are estimated from the minimum and maximum values of Φ^* allowed by the 1, 2, and 3 σ confidence contours in the $\alpha - M^*$ parameter space, respectively.

3.3. Uncertainties due to Photometric Redshift Errors

Studies of high-redshift galaxies still largely rely on photometric redshift estimates. It is therefore important to understand how the photometric redshift uncertainties affect the derived LF and to quantify the systematic effects on the LF best-fit parameters.

Chen et al. (2003) have shown that at lower redshifts ($z \lesssim 1$) the measurement of the LF is strongly affected by errors associated with z_{phot} . Specifically, large redshift errors together with the steep slope at the bright end of the galaxy LF tend to flatten the observed LF and result in measured M^* systematically brighter than the intrinsic value, since there are more intrinsically faint galaxies scattered into the bright end of the LF than intrinsically bright galaxies scattered into the faint end. Using Monte Carlo simulations, Chen et al. (2003) obtained a best-fit M^* that was 0.8 mag brighter than the intrinsic value in the redshift range $0.5 \leq z \leq 0.8$.

In order to quantify the systematic effect on the LF parameters α and M^* in our redshift range of interest ($2 \leq z \leq 3.5$), we performed a series of Monte Carlo simulations. The details of these simulations and the results are presented in Appendix A. Briefly, we generated several model catalogs of galaxies of different brightness according to an input Schechter LF, extracted the redshifts of the objects from a probability distribution proportional to the comoving volume per unit redshift (dV/dz), and obtained the final mock catalogs after applying a limit in the observed apparent magnitude. To simulate the errors in the redshifts, we assumed a redshift error function parametrized as a Gaussian distribution function of 1σ width $\sigma'_z(1+z)$, with σ'_z being the scatter in $\Delta z/(1+z_{spec})$, and we formed the observed redshift catalog by perturbing the input galaxy redshift within the redshift error function. Finally, we determined the LF for the galaxies at $z_1 \leq z \leq z_2$ using the $1/V_{max}$ and maximum likelihood methods described in §§ 3.1 and 3.2, respectively. As shown in Appendix A, the systematic effects on the measured α and M^* in the redshift interval $2 \leq z \leq 3.5$ are negligible with respect to the other uncertainties in the LF estimate if the errors on the photometric redshifts are characterized by a scatter in $\Delta z/(1+z_{spec})$ of $\sigma'_z \sim 0.12$, which is the appropriate value for the $z \geq 2$ sample considered in this work. This is not true at $z < 1$, where we find large systematic effects on both M^* and α , consistent with Chen et al. (2003). As explained in detail in Appendix A, the large systematic effects found at $z < 1$ arise from the strong redshift dependency of both dV/dz and dM/dz at low- z ; at $z > 2$ these dependencies are much less steep, and this results in smaller systematic effects on the measured LF. From the Monte Carlo simulations we also quantified that the effects of photometric redshift errors on the estimated luminosity density are typically a few percent (always $< 6\%$).

We conclude that the parameters of the LF and the luminosity density estimates presented in this work are not significantly affected by the uncertainties in the photometric redshift estimates⁸. In order to include this contribution in the error budget, we conservatively assume a 10% error contribution to the luminosity density error budget due to uncertainties in the photometric redshift estimates.

⁸ In Appendix A we also investigated the effects of non-Gaussian redshift error probability distributions. Systematic outliers in the photometric redshift distribution can potentially cause systematic errors in the LF measurements, although these are much smaller than the random uncertainties in the LF estimates (if the outliers are randomly distributed).

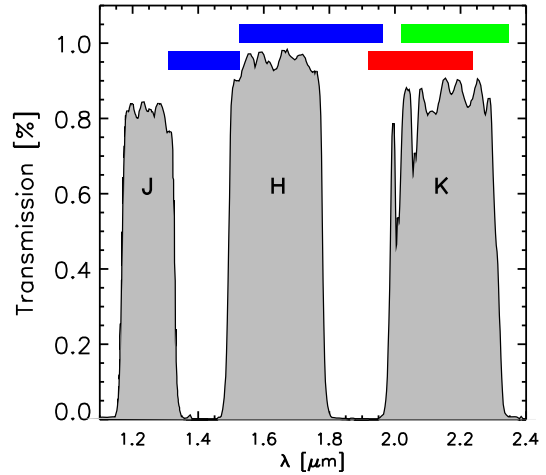


FIG. 2.— Transmission curves of the J , H , and K_s bands (gray shaded regions). The filled rectangles represent the observed wavelength ranges spanned by the central wavelengths of the rest-frame R band at $2 \leq z \leq 2.5$ (red), of the rest-frame V band at $2.7 \leq z \leq 3.3$ (green), and of the rest-frame B band at $2 \leq z \leq 2.5$ and $2.5 < z \leq 3.5$ (blue; lower and upper rectangles, respectively). For the considered redshift intervals, the rest-frame R and V bands correspond approximately to the observed K_s band.

4. THE OBSERVED LUMINOSITY FUNCTIONS

In this section we present the results of the measurement of the LF of galaxies at $z \geq 2$. We have measured the global LF in the rest-frame R and V band at redshift $2 \leq z \leq 2.5$ and $2.7 \leq z \leq 3.3$, respectively. As shown in Figure 2, at these redshifts, the rest-frame R and V bands correspond approximately to the observed K_s band, which is the selection band of the composite sample. We also measured the global LF in the rest-frame B band in the redshift interval $2 \leq z \leq 2.5$, to compare it with the rest-frame R -band LF, and at redshift $2.5 < z \leq 3.5$, to compare it with previous studies. For each redshift interval and rest-frame band we also split the sample based on the *observed* $J-K$ color ($J-K > 2.3$, DRGs; $J-K \leq 2.3$, non-DRGs) and the *rest-frame* $U-V$ color ($U-V \geq 0.25$, red galaxies; $U-V < 0.25$, blue galaxies). In § 4.1 we present the global LF of all galaxies, and in § 4.2 we present the LFs of the considered subsamples (DRGs, non-DRGs, red and blue galaxies) in the rest-frame R band. The results for the rest-frame V and B bands are shown in Appendix B; in Appendix C we compare our results with those in the literature.

4.1. Rest-Frame LF of All Galaxies

Figure 3 shows the global rest-frame R - and B -band LFs for galaxies at $2 \leq z \leq 2.5$, the rest-frame V -band LF at $2.7 \leq z \leq 3.3$, and the rest-frame B -band LF at $2.5 < z \leq 3.5$. The large surveyed area of the composite sample allows the determination of the bright end of the optical LF at $z \geq 2$ with unprecedented accuracy, while the depth of FIRES allows us to constrain also the faint-end slope. This is particularly important because of the well-known correlation between the two parameters α and M^* . The best-fit parameters with their 1, 2 and 3 σ errors (from the maximum likelihood analysis) are listed in Table 2, together with the Schechter parameters of the local rest-frame R -band (from Blanton et al. 2003) and B -band (from Norberg et al. 2002) LFs.

At redshift $2 \leq z \leq 2.5$, the faint-end slope of the rest-frame R -band LF is slightly flatter than in the rest-frame B -band, although the difference is within the errors. In the two higher redshift bins, the faint-end slope of the rest-frame V -band LF is flatter (by ~ 0.3) than in the rest-frame B -band, although

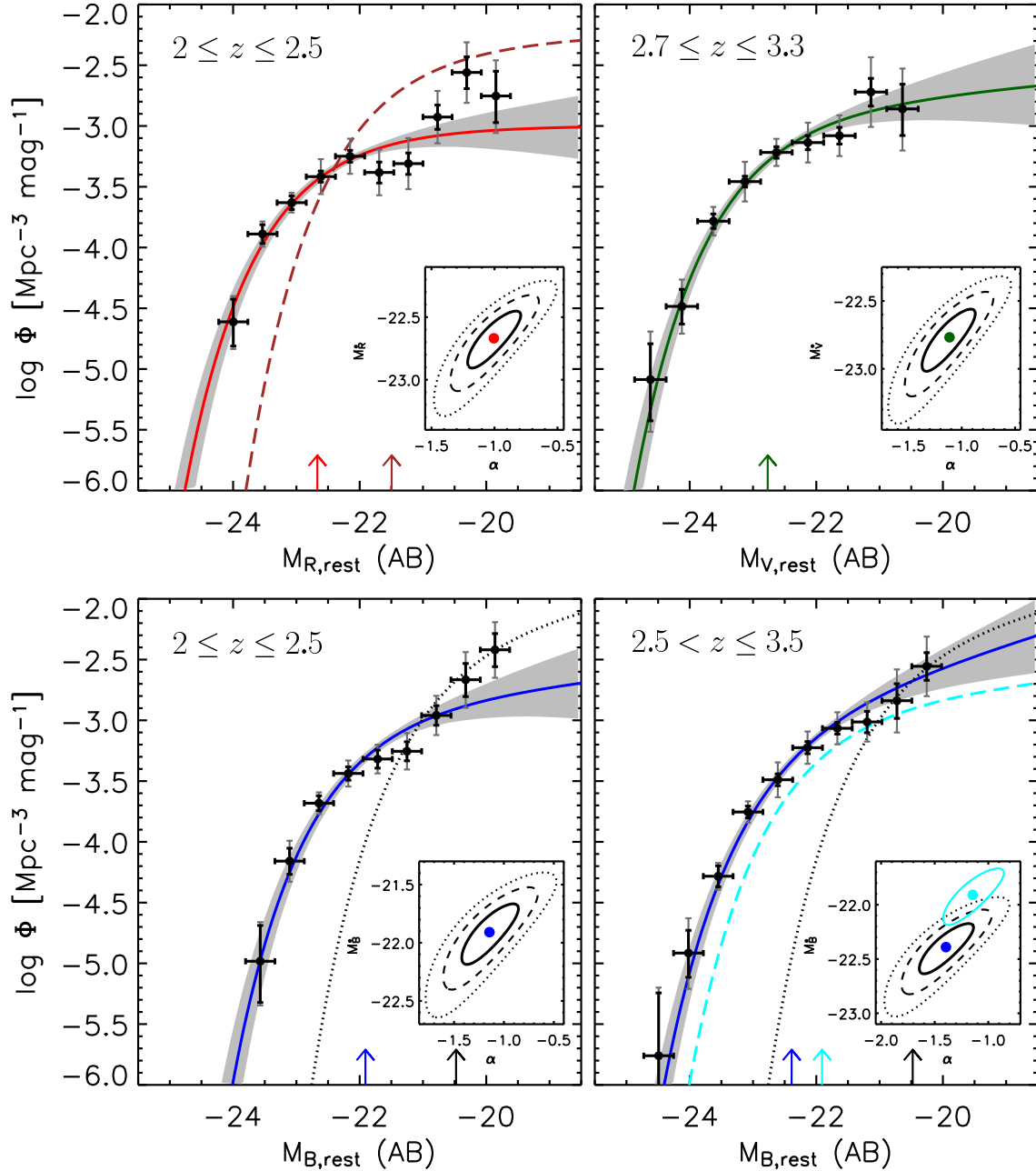


FIG. 3.— *Top left*: Rest-frame R -band LF at $2 \leq z \leq 2.5$ for all galaxies; black filled circles are the $1/V_{\max}$ method estimates with 1σ error bars (Poisson errors only in black; field-to-field variation term included in gray); the red solid line is the LF estimated from the maximum likelihood method, and the red arrow represents the best-fit M^* ; the shaded region represents the 1σ uncertainties of the LF estimated from the maximum likelihood method; the brown dashed line and arrow represent the local R -band LF from SDSS (Blanton et al. 2003; $R = r - 0.12$); the inset shows the best-fit value and the 1, 2, and 3 σ confidence contour levels of the two parameters α and M^* . *Top right*: Rest-frame V -band global LF at $2.7 \leq z \leq 3.3$; the dark green solid line and the arrow represent the LF from the maximum likelihood method. *Bottom left*: Rest-frame B -band global LF at $2 \leq z \leq 2.5$; the blue solid line and the arrow represent the LF from the maximum likelihood method; the black dotted line and arrow represent the local B -band LF from the 2dFGRS (Norberg et al. 2002; $B = b_1 + 0.12$). *Bottom right*: Rest-frame B -band global LF at $2.5 < z \leq 3.5$; the cyan dashed line and arrow represent the rest-frame B -band LF of all galaxies at $2 \leq z \leq 2.5$ for comparison; the black dotted line and arrow represent the local B -band LF from the 2dFGRS; in the inset, the 1σ confidence level of the estimated rest-frame B -band LF at $2 \leq z \leq 2.5$ is also plotted.

the difference is only at the 1σ level. Similarly, the faint-end slopes of the rest-frame B -band global LF in the low- and high-redshift bins are statistically identical. The characteristic magnitude M_B^* in the low- z interval is about 0.5 mag fainter with respect to the high-redshift one, although the difference is significant only at the $\sim 1.5 \sigma$ level. We therefore conclude that the rest-frame B -band global LFs in the low- and high-redshift bins are consistent with no evolution within their er-

rors ($< 2 \sigma$).

In Figure 3 we have also plotted the local ($z \sim 0.1$) rest-frame R -band (from Blanton et al. 2003) and B -band (from Norberg et al. 2002) LFs. The faint-end slope of the R -band LF at $2 \leq z \leq 2.5$ is very similar to the faint-end slope of the local LF; the characteristic magnitude is instead significantly ($> 3 \sigma$) brighter than the local value (by ~ 1.2 mag), and the characteristic density is a factor of ~ 4.8 smaller than the local

TABLE 2
BEST-FIT SCHECHTER FUNCTION PARAMETERS FOR THE GLOBAL LFs

Redshift Range	Rest-Frame Band	M^* (AB)	α	Φ^* ($10^{-4} \text{ Mpc}^{-3} \text{ mag}^{-1}$)
$2.0 \leq z \leq 2.5$	R	$-22.67^{+0.20,0.35,0.45}$	$-1.01^{+0.21,0.35,0.49}$	$10.65^{+2.65,4.50,5.92}$
$z = 0$	R	-21.50 ± 0.01	-1.05 ± 0.01	51.1 ± 1.4
$2.7 \leq z \leq 3.3$	V	$-22.77^{+0.20,0.33,0.45}$	$-1.12^{+0.23,0.40,0.57}$	$15.07^{+4.12,6.84,9.45}$
$2.0 \leq z \leq 2.5$	B	$-21.91^{+0.22,0.39,0.51}$	$-1.15^{+0.28,0.48,0.66}$	$14.57^{+4.60,8.07,11.07}$
$2.5 < z \leq 3.5$	B	$-22.39^{+0.20,0.35,0.45}$	$-1.40^{+0.25,0.42,0.58}$	$13.56^{+4.69,8.38,11.49}$
$z = 0$	B	-20.48 ± 0.07	-1.24 ± 0.03	62.9 ± 3.1

NOTE. — The quoted errors correspond to the 1, 2, and 3 σ errors estimated from the maximum likelihood analysis as described in § 3.2. The $z = 0$ values are the Schechter parameters of the local rest-frame R -band (from Blanton et al. 2003) and B -band (from Norberg et al. 2002) LFs. We assumed $R_{AB} = r - 0.12$ and $B_{AB} = b_j + 0.12$ to convert the local values into our photometric system.

value. The rest-frame B -band LF at $2.5 < z \leq 3.5$ is characterized by a faint-end slope consistent with the local B -band LF; the characteristic magnitude is significantly brighter ($> 3 \sigma$) than the local value by ~ 1.9 mag, while the characteristic density is a factor of ~ 4.6 smaller with respect to the local value.

4.2. Rest-Frame LF of DRGs, Non-DRGs, and Red and Blue Galaxies

In this section we present the results of the LFs for different subsamples, by splitting the composite sample based on the observed $J-K$ color ($J-K > 2.3$, DRGs; Franx et al. 2003) and on the rest-frame $U-V$ color (by defining the red galaxies as those having $U-V \geq 0.25$, which is the median value of $U-V$ of the composite sample at $2 \leq z \leq 2.5$). In Figure 4, we show the rest-frame $U-V$ color versus the observed $J-K$ color for the composite sample at $2 \leq z \leq 3.5$.

In Figure 5 we show the rest-frame R -band LF at $2 \leq z \leq 2.5$ of DRGs versus non-DRGs and red versus blue galaxies, together with the 1, 2, and 3 σ contour levels in the $\alpha - M_{R,AB}^*$ parameter space from the STY analysis. The LFs of the different subsamples in the rest-frame V band at $2.7 \leq z \leq 3.3$ and in the rest-frame B band at $2 \leq z \leq 2.5$ and $2.5 < z \leq 3.5$

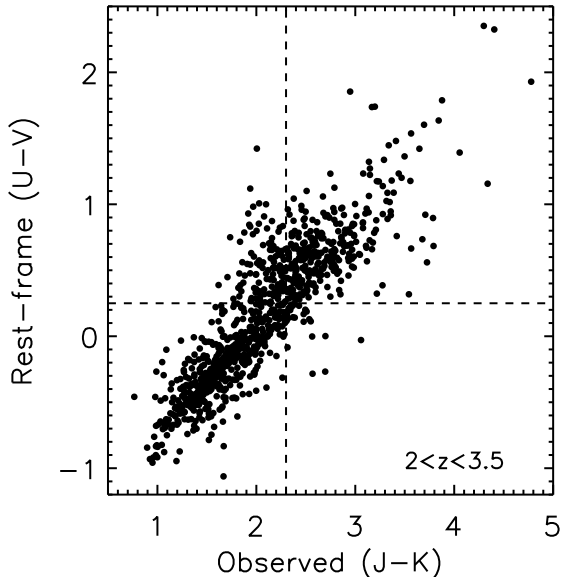


FIG. 4.— Rest-frame $U-V$ color vs. observed $J-K$ color for the composite sample at $2 \leq z \leq 3.5$; the dashed vertical line represents the $J-K > 2.3$ selection of DRGs, while the horizontal dashed line shows the $U-V \geq 0.25$ definition of red galaxies adopted in this paper.

are shown in Appendix B in Figures. B1, B2, and B3, respectively. In Table 3 the best-fit parameters and their 1, 2, and 3 σ errors from the STY method are listed for all the considered rest-frame bands and redshift intervals.

As shown in Figure 5, the rest-frame R -band LF at $2 \leq z \leq 2.5$ of DRGs is significantly ($> 3 \sigma$) different from that of non-DRGs. The faint-end slope of the non-DRG LF is much steeper, indicating that the contribution of DRGs to the global luminosity and number density at faint luminosities is very small compared to that of non-DRGs. The bright end of the DRG LF is instead very similar to that of non-DRGs, with the two subsamples contributing equally to the global LF. Splitting the composite sample based on the rest-frame $U-V$ color, we find a qualitatively similar result, with the faint-end slope of the blue galaxy LF being much steeper than that of red galaxies (although the red galaxies clearly dominate the bright end of the LF). The difference between the LFs of DRGs (red galaxies) and non-DRGs (blue galaxies) is mainly driven by the different faint-end slopes.

A similar result holds in the rest-frame V band at $2.7 \leq z \leq 3.3$, although it is slightly less significant (at the 2-3 σ level): the non-DRG (blue galaxy) LF is very similar to that of DRGs (red galaxies) at the bright end, while at the faint end, the LF of non-DRGs (blue galaxies) is steeper than that of DRGs (red galaxies). In the rest-frame B band, the differences between the LFs of DRGs/red galaxies and non-DRGs/blue galaxies become even less significant. Although DRGs/red galaxies are always characterized by LFs with flatter faint-end slopes, the significance of this result is only marginal ($< 2 \sigma$), especially in the higher redshift interval.

Within our sample, there is marginal evidence for evolution with redshift: the rest-frame B -band non-DRG/blue galaxy LFs in the two targeted redshift bins are characterized by similar (within the errors) faint-end slopes, while the characteristic magnitude is brighter by $\sim 0.5 - 0.6$ mag in the higher redshift bin. The LF of DRGs/red galaxies tends to get steeper from low to high redshifts and M^* gets brighter by ~ 0.6 mag. However, because of the large uncertainties (especially for DRGs and red galaxies) on the measured Schechter parameters, the differences in the rest-frame B band between the high- and the low-redshift bins are at most at the 2 σ significance level.

We note that the uncertainties on the estimated Schechter parameters mainly arise from the small number statistics at the very faint end, which is probed only by FIRES. Very deep (down to the deepest FIRES) NIR imaging over large spatially disjoint fields is required for further progress in our understanding of the lowest luminosity galaxies at $z > 2$.

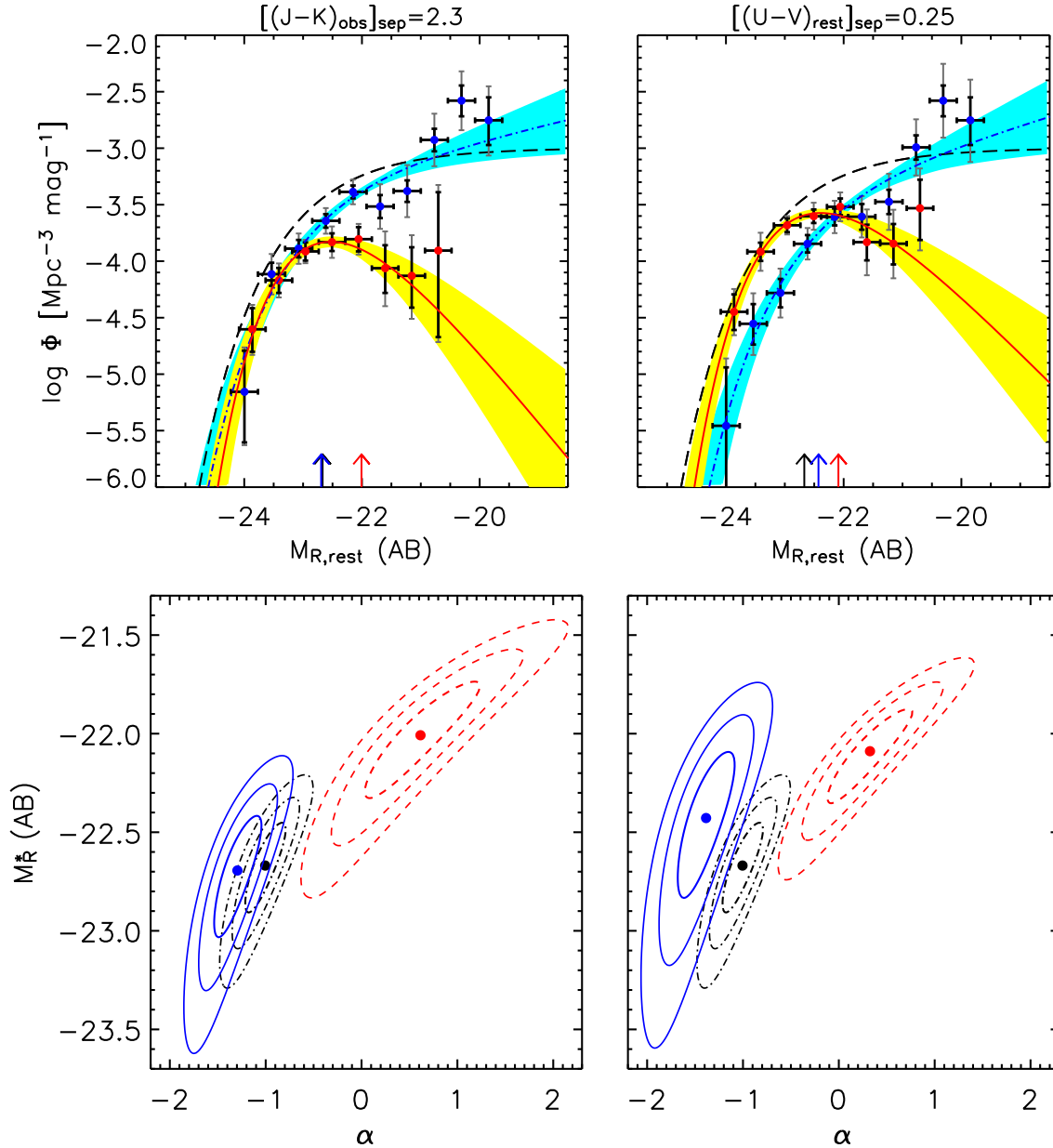


FIG. 5.— Rest-frame R-band LF at $2 \leq z \leq 2.5$. *Top*: Rest-frame R-band LFs at $2 \leq z \leq 2.5$ for DRGs/non-DRGs (*left*) and red/blue galaxies (*right*). The red solid line and filled circles represent the LF of DRGs and red galaxies estimated with the STY and $1/V_{\text{max}}$ methods, respectively; the blue dot-dashed line and filled circles represent the LF of non-DRGs and blue galaxies. The rest-frame R-band LF of all galaxies is also plotted (*black dashed line*). The shaded region (yellow for DRGs/red galaxies, cyan for non-DRGs/blue galaxies) represents the 1σ uncertainties of the LF measured with the STY method. The arrows represent the best-fit M^* ; error bars as in Fig. 3. *Bottom*: 1, 2, and 3 σ contour levels from the STY method for DRGs and red galaxies (*red dashed lines*), for non-DRGs and blue galaxies (*blue solid lines*), and for all galaxies (*black dot-dashed lines*); the filled circles represent the best-fit Schechter values. The LF of non-DRGs (blue galaxies) is steeper than that of DRGs (red galaxies).

4.3. Comparison with LBGs

Shapley et al. (2001) computed the rest-frame optical (V band) LF of $z \sim 3$ LBGs using the distribution of optical \mathcal{R} magnitudes (i.e., the rest-frame UV LF) and the distribution of $\mathcal{R}-K_s$ colors as a function of \mathcal{R} magnitude. The rest-frame UV LF of LBGs was taken from Adelberger & Steidel (2000) with best-fit Schechter parameters $\alpha = -1.57 \pm 0.11$, $M_{\mathcal{R}}^* = 24.54 \pm 0.14$ mag, and $\Phi^* = (1.5 \pm 0.4) \times 10^{-3}$ Mpc $^{-3}$ in our adopted cosmology. Shapley et al. (2001) detected a correlation with 98% confidence between $\mathcal{R}-K_s$ color and \mathcal{R} magnitude, such that fainter galaxies have redder $\mathcal{R}-K_s$ colors. This trend was included in their LF analysis by using the relationship implied by the best-fit regression slope to the correlation, $d\langle \mathcal{R}-K_s \rangle / d\mathcal{R} = 0.17$ (the scatter around this

regression is very large). The Schechter function was then fitted to the average LF values, obtaining best-fit Schechter parameters $\alpha = -1.85 \pm 0.15$, $M_{V,AB}^* = -22.99 \pm 0.25$ mag, and $\Phi^* = (6.2 \pm 2.7) \times 10^{-4}$ Mpc $^{-3}$. The overall shape of the rest-frame optical LF of LBGs is determined by the way in which the $\mathcal{R}-K_s$ distribution as a function of \mathcal{R} magnitude redistributes \mathcal{R} magnitudes into K_s magnitudes. Therefore, as a result of the detected positive correlation between \mathcal{R} and $\mathcal{R}-K_s$, the faint-end slope of the LBG rest-frame optical LF is steeper than that of the UV LF (Shapley et al. 2001).

In Figure 6 we compare the rest-frame V -band LF of blue galaxies at $2.7 \leq z \leq 3.3$ and the LBG LF from Shapley et al. (2001) in the same rest-frame band and redshift interval. The blue galaxy LF estimated with the $1/V_{\text{max}}$ method ap-

TABLE 3
BEST-FIT SCHECHTER FUNCTION PARAMETERS FOR SUBSAMPLES

Redshift Range	Rest-Frame Band	Sample	M^* (AB)	α	Φ^* ($10^{-4} \text{ Mpc}^{-3} \text{ mag}^{-1}$)
$2.0 \leq z \leq 2.5$	R	$J-K > 2.3$	$-22.01^{+0.26,0.43,0.57}_{-0.30,0.55,0.81}$	$0.62^{+0.62,1.07,1.54}_{-0.57,0.92,1.24}$	$3.74^{+0.69,1.02,1.37}_{-1.09,1.90,2.58}$
		$J-K \leq 2.3$	$-22.69^{+0.27,0.43,0.57}_{-0.33,0.60,0.93}$	$-1.30^{+0.24,0.41,0.57}_{-0.24,0.40,0.55}$	$6.32^{+2.72,4.59,6.30}_{-2.41,3.76,4.78}$
		$U-V \geq 0.25$	$-22.09^{+0.20,0.35,0.47}_{-0.24,0.45,0.65}$	$0.33^{+0.43,0.76,1.09}_{-0.44,0.70,0.95}$	$7.51^{+0.69,1.14,1.57}_{-1.14,2.19,3.31}$
		$U-V < 0.25$	$-22.43^{+0.32,0.51,0.69}_{-0.40,0.75,1.15}$	$-1.39^{+0.29,0.49,0.68}_{-0.29,0.48,0.67}$	$5.26^{+2.97,4.97,7.32}_{-2.42,3.64,4.47}$
		$2.7 \leq z \leq 3.3$	V	$J-K > 2.3$	$-22.63^{+0.28,0.47,0.63}_{-0.36,0.65,0.99}$
$2.0 \leq z \leq 2.5$	B	$J-K \leq 2.3$	$-22.63^{+0.24,0.41,0.55}_{-0.32,0.57,0.87}$	$-1.21^{+0.30,0.50,0.71}_{-0.31,0.50,0.69}$	$11.14^{+4.02,7.12,9.88}_{-4.27,6.61,8.41}$
		$U-V \geq 0.25$	$-22.43^{+0.28,0.45,0.61}_{-0.32,0.59,0.87}$	$-0.11^{+0.60,1.02,1.46}_{-0.53,0.87,1.19}$	$6.25^{+0.87,1.54,2.24}_{-0.92,2.08,3.40}$
		$U-V < 0.25$	$-22.65^{+0.26,0.43,0.57}_{-0.30,0.57,0.85}$	$-1.26^{+0.31,0.51,0.73}_{-0.29,0.49,0.68}$	$11.01^{+4.50,7.72,10.55}_{-4.16,6.52,8.36}$
		$J-K > 2.3$	$-21.75^{+0.42,0.67,0.87}_{-0.54,1.03,1.73}$	$-0.54^{+0.73,1.25,1.79}_{-0.66,1.08,1.47}$	$4.12^{+1.29,2.18,3.18}_{-1.77,2.99,3.78}$
		$J-K \leq 2.3$	$-21.89^{+0.26,0.43,0.57}_{-0.32,0.59,0.89}$	$-1.25^{+0.31,0.53,0.73}_{-0.31,0.52,0.72}$	$11.08^{+4.52,7.83,10.92}_{-4.36,6.75,8.57}$
$2.5 < z \leq 3.5$	B	$U-V \geq 0.25$	$-21.63^{+0.30,0.49,0.65}_{-0.38,0.69,1.05}$	$-0.40^{+0.57,0.99,1.41}_{-0.56,0.91,1.24}$	$8.63^{+1.57,2.70,3.95}_{-2.33,4.35,6.20}$
		$U-V < 0.25$	$-21.83^{+0.32,0.51,0.67}_{-0.42,0.77,1.19}$	$-1.33^{+0.34,0.58,0.81}_{-0.35,0.58,0.81}$	$8.19^{+4.47,7.70,10.97}_{-3.94,5.83,7.09}$
		$J-K > 2.3$	$-22.35^{+0.32,0.51,0.67}_{-0.38,0.73,1.17}$	$-1.11^{+0.51,0.86,1.21}_{-0.49,0.81,1.14}$	$4.88^{+2.09,3.35,4.55}_{-2.20,3.48,4.32}$
		$J-K \leq 2.3$	$-22.35^{+0.26,0.43,0.57}_{-0.30,0.57,0.87}$	$-1.45^{+0.30,0.51,0.71}_{-0.29,0.48,0.67}$	$9.50^{+3.92,6.04,7.57}_{-2.05,3.25,4.49}$
		$U-V \geq 0.25$	$-22.25^{+0.32,0.51,0.67}_{-0.38,0.75,1.17}$	$-1.01^{+0.55,0.92,1.31}_{-0.52,0.87,1.21}$	$5.37^{+2.34,3.77,4.73}_{-4.33,7.60,10.84}$
$U-V < 0.25$	$-22.41^{+0.26,0.43,0.57}_{-0.30,0.57,0.87}$	$-1.49^{+0.30,0.50,0.70}_{-0.27,0.47,0.65}$	$8.80^{+3.64,5.62,7.00}_{-3.64,5.62,7.00}$		

NOTE. — The quoted errors correspond to the 1, 2, and 3 σ errors estimated from the maximum likelihood analysis as described in § 3.2.

pears consistent within the errors with the average LF values of LBGs (shown as stars in Figure 6). However, the best-fit Schechter parameters from the maximum likelihood analysis are only marginally consistent, with the faint-end slope of the LBG LF being significantly steeper than the one of blue galaxies, as shown in the inset of Figure 6. The same result is obtained if the rest-frame V -band LF of non-DRGs (rather than rest-frame blue galaxies) is compared to that of LBGs.

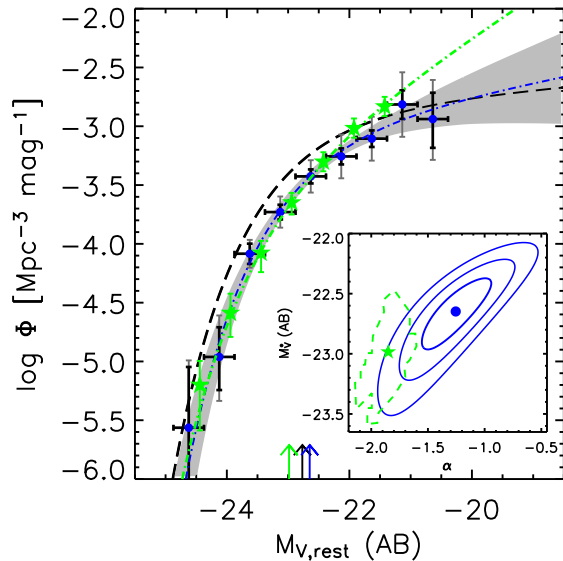


FIG. 6.— Rest-frame V -band LF of blue galaxies at redshift $2.7 \leq z \leq 3.3$ (blue dot-dashed line and filled circles) and $z \sim 3$ LBG LF (Shapley et al. 2001) (green dot-dashed and filled stars); the shaded area represents the 1σ uncertainties of the blue galaxy LF measured with the STY method; the global LF measured with the STY method is also plotted as a black long-dashed line; arrows represent the best-fit M^* . The inset shows the best-fit value and the 1, 2, and 3 σ confidence contour levels of the two parameters α and M^* for blue galaxies (blue filled circle and solid lines) and the 68.3% confidence intervals for the LBG best-fit Schechter parameters from (Shapley et al. 2001) (green filled star and dashed line).

4.4. Comparison with Previous Studies

In Appendix C we compare our results with previously published LFs. Specifically, we have compared our rest-frame B -band LF with that derived by Poli et al. (2003), Giallongo et al. (2005), and Gabasch et al. (2004) in the redshift intervals $2 \leq z \leq 2.5$ and $2.5 < z \leq 3.5$, and our rest-frame R -band LF with the rest-frame r -band LF derived by Gabasch et al. (2006) at $2 \leq z \leq 2.5$. We also compared our rest-frame B -band LFs of red and blue galaxies at $2.5 < z \leq 3.5$ with those measured by Giallongo et al. (2005).

5. DENSITIES

5.1. Number Density and Field-to-Field Variance

The estimates of the number density η obtained by integrating the best-fit Schechter function to the faintest observed rest-frame luminosities are listed in Table 4. For completeness, we also list η^{MUSYC} , calculated by integrating the best-fit Schechter LF to the rest-frame magnitude limits of the NIR MUSYC, and η^{+2} , calculated by integrating the best-fit Schechter LF to 2 mag fainter than the faintest observed luminosities. We find that the contribution of DRGs (red galaxies) to the total number density down to the faintest probed rest-frame luminosities is 13%-25% (18%-29%) depending on the redshift interval. By integrating the rest-frame B -band LF down to a fixed rest-frame magnitude limit ($M_{B,AB} = -20$), we find a hint of an increase of the contribution of blue galaxies from the low redshift bin (62%) to the higher bin (74%), but the differences are not significant. If only the bright end of the LF is considered (integrating the LF down to the fixed NIR MUSYC limit, $M_{B,AB} = -22.2$), the increase of the contribution of the blue galaxy population becomes significant at the 2σ level, going from 42% in the low- z bin to 66% in the high- z bin.

We determine the field-to-field variance in the density by fixing the parameters α and M^* to the best-fit values measured using the composite sample, and estimating Φ_j^* for each j th field separately by imposing a normalization on the LF such

TABLE 4
 NUMBER DENSITIES

Redshift Range	Rest-Frame Band	Sample	^a $\log \eta$ (Mpc ⁻³)	^b $\log \eta^{\text{MUSYC}}$ (Mpc ⁻³)	^c $\log \eta^{+2}$ (Mpc ⁻³)
2.0 ≤ z ≤ 2.5	R	All	-2.61 ^{+0.07,0.11,0.16} _{-0.06,0.10,0.13}	-3.18 ^{+0.02,0.03,0.04} _{-0.02,0.03,0.04}	-2.36 ^{+0.17,0.29,0.42} _{-0.13,0.20,0.27}
		J-K > 2.3	-3.48 ^{+0.07,0.14,0.21} _{-0.05,0.08,0.10}	-3.64 ^{+0.02,0.03,0.04} _{-0.02,0.03,0.04}	-3.48 ^{+0.09,0.19,0.31} _{-0.06,0.09,0.11}
		J-K ≤ 2.3	-2.63 ^{+0.08,0.14,0.20} _{-0.08,0.13,0.17}	-3.37 ^{+0.02,0.03,0.04} _{-0.03,0.05,0.07}	-2.24 ^{+0.25,0.42,0.59} _{-0.18,0.29,0.39}
		U-V ≥ 0.25	-3.19 ^{+0.07,0.12,0.17} _{-0.05,0.08,0.10}	-3.39 ^{+0.02,0.03,0.04} _{-0.02,0.03,0.04}	-3.18 ^{+0.09,0.17,0.28} _{-0.06,0.09,0.11}
		U-V < 0.25	-2.72 ^{+0.10,0.16,0.22} _{-0.09,0.14,0.20}	-3.59 ^{+0.03,0.05,0.06} _{-0.04,0.08,0.11}	-2.25 ^{+0.31,0.52,0.73} _{-0.21,0.34,0.46}
2.7 ≤ z ≤ 3.3	V	All	-2.51 ^{+0.07,0.11,0.16} _{-0.06,0.10,0.14}	-3.27 ^{+0.02,0.03,0.05} _{-0.03,0.05,0.07}	-2.16 ^{+0.19,0.33,0.47} _{-0.15,0.24,0.32}
		J-K > 2.3	-3.17 ^{+0.12,0.21,0.30} _{-0.10,0.16,0.20}	-3.65 ^{+0.02,0.03,0.04} _{-0.03,0.06,0.10}	-3.05 ^{+0.26,0.50,0.76} _{-0.17,0.25,0.31}
		J-K ≤ 2.3	-2.63 ^{+0.08,0.13,0.18} _{-0.07,0.12,0.16}	-3.49 ^{+0.03,0.05,0.06} _{-0.04,0.07,0.11}	-2.22 ^{+0.24,0.41,0.59} _{-0.19,0.30,0.40}
		U-V ≥ 0.25	-3.25 ^{+0.11,0.20,0.28} _{-0.09,0.14,0.18}	-3.65 ^{+0.02,0.03,0.04} _{-0.03,0.05,0.08}	-3.19 ^{+0.26,0.50,0.76} _{-0.13,0.19,0.24}
		U-V < 0.25	-2.61 ^{+0.08,0.13,0.18} _{-0.07,0.12,0.16}	-3.49 ^{+0.03,0.05,0.07} _{-0.04,0.07,0.11}	-2.17 ^{+0.24,0.41,0.59} _{-0.20,0.32,0.41}
2.0 ≤ z ≤ 2.5	B	All	-2.53 ^{+0.08,0.12,0.17} _{-0.08,0.13,0.19}	-3.38 ^{+0.03,0.05,0.06} _{-0.03,0.06,0.09}	-2.15 ^{+0.25,0.42,0.60} _{-0.17,0.28,0.37}
		J-K > 2.3	-3.34 ^{+0.17,0.30,0.42} _{-0.13,0.21,0.27}	-3.92 ^{+0.04,0.05,0.07} _{-0.05,0.11,0.17}	-3.19 ^{+0.42,0.80,1.23} _{-0.23,0.33,0.40}
		J-K ≤ 2.3	-2.60 ^{+0.09,0.15,0.21} _{-0.08,0.14,0.19}	-3.53 ^{+0.04,0.06,0.07} _{-0.05,0.08,0.12}	-2.17 ^{+0.30,0.51,0.73} _{-0.20,0.33,0.43}
		U-V ≥ 0.25	-3.07 ^{+0.13,0.23,0.33} _{-0.11,0.17,0.22}	-3.63 ^{+0.03,0.04,0.06} _{-0.04,0.08,0.12}	-2.95 ^{+0.29,0.58,0.88} _{-0.18,0.26,0.32}
		U-V < 0.25	-2.71 ^{+0.10,0.16,0.23} _{-0.09,0.15,0.21}	-3.71 ^{+0.04,0.07,0.09} _{-0.06,0.10,0.16}	-2.23 ^{+0.35,0.59,0.83} _{-0.22,0.37,0.49}
2.5 < z ≤ 3.5	B	All	-2.43 ^{+0.07,0.12,0.17} _{-0.07,0.12,0.16}	-3.46 ^{+0.03,0.05,0.06} _{-0.04,0.06,0.09}	-1.92 ^{+0.23,0.39,0.54} _{-0.18,0.30,0.40}
		J-K > 2.3	-3.04 ^{+0.15,0.26,0.36} _{-0.14,0.22,0.29}	-3.89 ^{+0.04,0.07,0.09} _{-0.06,0.12,0.19}	-2.68 ^{+0.42,0.76,1.10} _{-0.32,0.47,0.58}
		J-K ≤ 2.3	-2.57 ^{+0.08,0.14,0.19} _{-0.08,0.13,0.18}	-3.65 ^{+0.04,0.06,0.08} _{-0.04,0.08,0.12}	-2.03 ^{+0.27,0.46,0.65} _{-0.22,0.35,0.47}
		U-V ≥ 0.25	-3.06 ^{+0.16,0.27,0.38} _{-0.14,0.22,0.29}	-3.90 ^{+0.05,0.07,0.09} _{-0.07,0.12,0.20}	-2.74 ^{+0.44,0.78,1.14} _{-0.31,0.45,0.56}
		U-V < 0.25	-2.56 ^{+0.08,0.14,0.19} _{-0.08,0.13,0.18}	-3.64 ^{+0.04,0.06,0.08} _{-0.04,0.08,0.12}	-2.00 ^{+0.26,0.45,0.64} _{-0.22,0.35,0.47}

^aThe number densities are estimated by integrating the best-fit Schechter LF down to the faintest observed rest-frame luminosities: $M_{R,AB}^{\text{last}} = -19.6$, $M_{V,AB}^{\text{last}} = -20.3$ and $M_{B,AB}^{\text{last}} = -19.5$, $M_{B,AB}^{\text{last}} = -20.0$ for the low- and high-redshift intervals, respectively; they correspond to observed K_s band magnitude of $K_s^{\text{tot}} \approx 23.14$ at the lower limit of the targeted redshift intervals. The quoted errors correspond to the 1, 2, and 3 σ errors estimated from the maximum likelihood analysis as described in § 3.2.

^b η^{MUSYC} is the number density estimated by integrating the best-fit Schechter LF down to the rest-frame magnitude limits of the deep NIR MUSYC survey: $M_{R,AB}^{\text{MUSYC}} = -21.8$, $M_{V,AB}^{\text{MUSYC}} = -22.4$ and $M_{B,AB}^{\text{MUSYC}} = -21.7$, -22.2 for the low- and high-redshift intervals, respectively (corresponding to observed $K_s^{\text{tot}} \approx 21.09$).

^c η^{+2} is the number density estimated by integrating the best-fit Schechter LF down to 2 mag fainter than the faintest observed luminosities.

that the total number of observed galaxies in each field is reproduced. In Table 5, the derived Φ_j^* of DRGs and non-DRGs in each field are listed for the three targeted redshift intervals and compared to Φ^* measured from the composite sample. The results in the redshift range $2.5 < z < 3.5$ are plotted in Figure 7. We find an overdensity of DRGs in the M1030 field at all redshifts, with the excess (as compared to the characteristic density of the composite sample) varying from a factor of ~ 1.2 in the lowest redshift bin up to a factor of ~ 1.9 in the redshift interval $2.5 < z < 3.5$. We also find an underdensity of DRGs (a factor of 0.82-0.86) in the GOODS-CDFS field, although only at $z > 2.5$. The value of Φ^* for DRGs in M1030 is a factor of ~ 1.6 -2.4 larger than that in the GOODS-CDFS field at $z > 2.5$, although they are similar at $2 \leq z \leq 2.5$.

These results are qualitatively consistent with van Dokkum et al. (2006), who showed that the GOODS-CDFS field is underdense in massive ($M_* > 10^{11} M_\odot$) galaxies at $2 < z < 3$, with a surface density that is about 60% of the mean and a factor of 3 lower than that of their highest density field (M1030). However, our results seem to show systematically smaller underdensities for the GOODS-CDFS field compared to their work. In order to understand the origin of the smaller underdensities for the GOODS-CDFS field compared to their work. In order to understand the origin of the smaller underdensities of DRGs found for the GOODS-CDFS field in our work compared to that of massive galaxies in van Dokkum et al. (2006), we have estimated the surface density of DRGs in the redshift range $2 < z < 3$ down to $K_s^{\text{tot}} = 21$. We find

that the surface density of DRGs in the GOODS-CDFS field is $\sim 70\%$ of the mean and a factor of $\sim 2.2 \pm 0.5$ lower than that of the M1030 field, in good agreement with the values

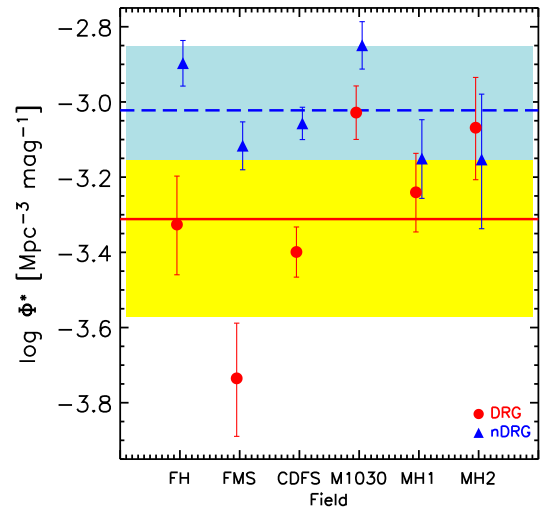


FIG. 7.— Values of Φ^* for DRGs (red filled circles) and non-DRGs (blue filled triangles) in the redshift range $2.5 < z < 3.5$ estimated in the rest-frame B band as described in § 5.1 for each individual field; the yellow (DRGs) and cyan (non-DRGs) shaded regions represent the values of Φ^* from the analysis in § 3.2 on the composite sample.

TABLE 5
CHARACTERISTIC DENSITY Φ^* IN EACH FIELD

Redshift Range	Composite Sample	MH2	MH1	M1030	CDFS	FMS	FH
DRGs							
$2.0 \leq z \leq 2.5$	$3.74^{+0.69}_{-1.09}$	$2.71^{+0.93}_{-0.73}$	$3.13^{+0.76}_{-0.62}$	$4.49^{+0.83}_{-0.71}$	$3.96^{+0.83}_{-0.70}$	$3.78^{+1.51}_{-1.12}$	$6.14^{+4.84}_{-2.93}$
$2.7 \leq z \leq 3.3$	$6.14^{+1.10}_{-1.71}$	$7.41^{+2.26}_{-1.78}$	$6.45^{+1.43}_{-1.19}$	$8.49^{+1.46}_{-1.26}$	$5.25^{+0.94}_{-0.81}$	$2.70^{+1.23}_{-0.88}$	$7.79^{+3.84}_{-2.69}$
$2.5 < z \leq 3.5$	$4.88^{+2.09}_{-2.20}$	$8.54^{+3.08}_{-2.33}$	$5.75^{+1.55}_{-1.24}$	$9.37^{+1.66}_{-1.42}$	$3.99^{+0.66}_{-0.57}$	$1.84^{+0.74}_{-0.55}$	$4.72^{+1.63}_{-1.25}$
non-DRGs							
$2.0 \leq z \leq 2.5$	$6.32^{+2.72}_{-2.41}$	$6.26^{+1.55}_{-1.27}$	$8.63^{+1.24}_{-1.09}$	$7.90^{+1.09}_{-0.96}$	$3.22^{+0.53}_{-0.46}$	$5.80^{+1.07}_{-0.91}$	$12.65^{+2.33}_{-1.99}$
$2.7 \leq z \leq 3.3$	$11.14^{+4.02}_{-4.27}$	$11.49^{+3.80}_{-2.93}$	$13.44^{+2.44}_{-2.09}$	$13.52^{+2.17}_{-1.89}$	$9.65^{+1.14}_{-1.03}$	$6.70^{+1.46}_{-1.22}$	$18.68^{+3.35}_{-2.87}$
$2.5 < z \leq 3.5$	$9.50^{+4.33}_{-3.92}$	$7.03^{+3.46}_{-2.43}$	$7.07^{+1.90}_{-1.53}$	$14.15^{+2.30}_{-1.92}$	$8.77^{+0.91}_{-0.83}$	$7.65^{+1.20}_{-1.05}$	$12.68^{+1.89}_{-1.66}$

NOTE. — Units in $10^{-4} \text{ Mpc}^{-3} \text{ mag}^{-1}$; the 1σ error of the characteristic density estimated for the individual field includes only the Poisson error (Gehrels 1986). The measured rest-frame R -, V -, and B -band LFs have been used in the redshift ranges $2.0 \leq z \leq 2.5$, $2.7 \leq z \leq 3.3$, and $2.5 < z \leq 3.5$, respectively.

in van Dokkum et al. (2006). Therefore, the smaller underdensities of DRGs found for the GOODS-CDFS field in our work appear to arise mainly from the different targeted redshift ranges. The approach adopted in this work to quantify field-to-field variance by comparing the Φ_j^* of the individual fields might also mitigate field-to-field differences, especially at the bright end.

We note that there are significant differences in the observed characteristic densities even within the MUSYC fields, although they have areas of $\sim 100 \text{ arcmin}^2$. For example, the observed Φ^* of DRGs in the MH1 field is consistent with the one derived from the composite sample, but it is 0.61–0.76 times the value in the M1030 field. These results demonstrate that densities inferred from individual $\sim 100 \text{ arcmin}^2$ fields should be treated with caution.

5.2. Luminosity Density

In this section we present estimates of the luminosity density. Because of the coupling between the two parameters α and M^* , the luminosity density (obtained by integrating the LF over all magnitudes) is a robust way to characterize the contribution to the total LF from the different subpopulations and to characterize the evolution of the LF with redshift.

The luminosity density ρ_L is calculated using:

$$\rho_L = \int_0^\infty L_\nu \Phi(L_\nu) dL_\nu = \Gamma(2+\alpha) \Phi^* L^*, \quad (7)$$

which assumes that the Schechter parametrization of the observed LF is a good approximation and valid also at luminosities fainter than probed by our composite sample. Table 6 lists ρ_L with the corresponding 1, 2, and 3 σ errors⁹ for all of the considered samples. We also list ρ_L^{last} , the luminosity density calculated to the faintest probed rest-frame luminosity, and ρ_L^{MUSYC} , the luminosity density calculated to the rest-frame magnitude limits of the deep NIR MUSYC. While the difference between ρ_L and ρ_L^{last} is very small (negligible for DRGs and red galaxies, and ~ 0.1 dex on average for non-DRGs and blue galaxies), the difference between ρ_L and ρ_L^{MUSYC} is significant, especially for non-DRGs and blue galaxies (~ 0.5 dex on average).

⁹ The 1, 2, and 3 σ errors of the luminosity densities were calculated by deriving the distribution of all the values of ρ_L allowed within the 1, 2, and 3 σ solutions, respectively, of the Schechter LF parameters from the maximum likelihood analysis. The contribution from the uncertainties in the photometric redshift estimates derived in Appendix A was added in quadrature.

In the top panel of Figure 8 we have plotted the total rest-frame B -band luminosity density ρ_L versus the redshift, including a compilation of results from the literature. Only the results from the literature which are not significantly affected by field-to-field variations, or that have taken these into account, are plotted. Our measurement of the total rest-frame B -band luminosity density is the only one at $z > 2$ that is not significantly affected by field-to-field variance. From Figure 8, there is an indication of a possible increase of the total luminosity density in the highest redshift bin, significant at the $\sim 2.2 \sigma$ level. The measurement at $2 \leq z \leq 2.5$ is consistent with the one at $z \sim 1.9$ from Dahlen et al. (2005). In Figure 8 we have also plotted the computed B -band rest-frame luminosity density as a function of z predicted from large-scale Λ CDM hydrodynamical simulations from Nagamine et al. (2000, 2001) and from a semianalytical model taken from Dahlen et al. (2005). While the predicted luminosity densities match the measurements at $z \leq 1.2$ well, they clearly overpredict them at larger redshifts. Only the prediction at $z \sim 3$ from Nagamine et al. (2000) is consistent with our measurement, although their model still overpredicts significantly the luminosity densities in the range $1.2 \leq z \leq 2.5$.

The bottom panel of Figure 8 shows the total rest-frame R -band luminosity density ρ_L versus the redshift, including a compilation of results from the literature as in the top panel. As for the rest-frame B band, our measurement of the rest-frame R -band ρ_L is the first one at $z > 2$ for which sample variance does not significantly contribute to the error budget. Our point at $z > 2$ is consistent with the trend observed at $z < 2$ of decreasing luminosity densities with increasing redshifts, although the point at $z \sim 1.9$ from the LF analysis of the GOODS-CDFS survey by Dahlen et al. (2005) is only $\sim 43\%$ of our measurement at $z \sim 2.2$. From Table 5 we see that in the redshift range $2 \leq z \leq 2.5$, the CDFS field is underdense in non-DRGs. The value of Φ^* for all galaxies in the CDFS field is $6.67^{+0.83}_{-0.74} \times 10^{-4} \text{ Mpc}^{-3} \text{ mag}^{-1}$ (estimated as in § 5.1), which is a factor of $0.63^{+0.30}_{-0.18}$ the value of Φ^* from the composite sample (see Table 2). Therefore, the lower value of the rest-frame R -band ρ_L from Dahlen et al. (2005) at $1.8 < z < 2$ could be due to an underdensity of galaxies at $z \sim 2$. In Figure 8 we have also plotted the computed R -band rest-frame luminosity density as function of z predicted from large-scale Λ CDM hydrodynamical simulations from Nagamine et al. (2000). As for the rest-frame B band, the predictions match the observations well enough at $z \leq 1$, but at larger redshifts they significantly overpredict them.

TABLE 6
LUMINOSITY DENSITIES

Redshift Range	Rest-Frame Band	Sample	$\log \rho_L$	$\log \rho_L^{\text{last}^{\text{a}}}$	$\log \rho_L^{\text{MUSYC}^{\text{b}}}$
$2.0 \leq z \leq 2.5$	<i>R</i>	All	$26.74^{+0.06,0.08,0.12}_{-0.05,0.06,0.07}$	$26.71^{+0.05,0.06,0.07}_{-0.05,0.06,0.07}$	$26.53^{+0.05,0.06,0.07}_{-0.05,0.06,0.07}$
		$J-K > 2.3$	$26.18^{+0.05,0.06,0.08}_{-0.05,0.06,0.07}$	$26.18^{+0.05,0.06,0.08}_{-0.05,0.06,0.07}$	$26.14^{+0.05,0.07,0.09}_{-0.05,0.07,0.09}$
		$J-K \leq 2.3$	$26.64^{+0.10,0.20,0.43}_{-0.07,0.08,0.10}$	$26.57^{+0.05,0.06,0.07}_{-0.05,0.06,0.07}$	$26.30^{+0.06,0.08,0.10}_{-0.06,0.09,0.11}$
		$U-V \geq 0.25$	$26.43^{+0.05,0.06,0.07}_{-0.05,0.06,0.07}$	$26.43^{+0.05,0.06,0.07}_{-0.05,0.06,0.07}$	$26.37^{+0.05,0.06,0.07}_{-0.05,0.06,0.07}$
		$U-V < 0.25$	$26.50^{+0.18,0.48,2.47}_{-0.09,0.15,0.26}$	$26.40^{+0.05,0.06,0.08}_{-0.05,0.06,0.07}$	$26.03^{+0.07,0.10,0.13}_{-0.08,0.12,0.16}$
		$2.7 \leq z \leq 3.3$	<i>V</i>	All	$26.97^{+0.06,0.07,0.09}_{-0.07,0.12,0.24}$
$J-K > 2.3$	$26.44^{+0.05,0.06,0.07}_{-0.05,0.06,0.07}$			$26.43^{+0.05,0.06,0.07}_{-0.05,0.06,0.07}$	$26.26^{+0.06,0.08,0.10}_{-0.06,0.09,0.13}$
$J-K \leq 2.3$	$26.82^{+0.12,0.28,0.66}_{-0.07,0.10,0.12}$			$26.73^{+0.05,0.06,0.07}_{-0.05,0.06,0.07}$	$26.36^{+0.06,0.08,0.11}_{-0.07,0.10,0.13}$
$U-V \geq 0.25$	$26.40^{+0.05,0.06,0.07}_{-0.05,0.06,0.07}$			$26.39^{+0.05,0.06,0.07}_{-0.05,0.06,0.07}$	$26.26^{+0.06,0.08,0.11}_{-0.06,0.08,0.12}$
$U-V < 0.25$	$26.84^{+0.13,0.31,0.85}_{-0.08,0.11,0.13}$			$26.74^{+0.05,0.06,0.07}_{-0.05,0.06,0.07}$	$26.36^{+0.06,0.08,0.10}_{-0.07,0.10,0.13}$
$2.0 \leq z \leq 2.5$	<i>B</i>			All	$26.61^{+0.10,0.20,0.38}_{-0.07,0.09,0.11}$
		$J-K > 2.3$	$25.90^{+0.10,0.27,2.95}_{-0.06,0.07,0.08}$	$25.89^{+0.06,0.09,0.13}_{-0.05,0.06,0.07}$	$25.64^{+0.08,0.11,0.15}_{-0.09,0.15,0.22}$
		$J-K \leq 2.3$	$26.53^{+0.15,0.35,1.15}_{-0.08,0.11,0.13}$	$26.43^{+0.05,0.07,0.08}_{-0.05,0.06,0.07}$	$25.99^{+0.07,0.10,0.13}_{-0.07,0.12,0.16}$
		$U-V \geq 0.25$	$26.18^{+0.07,0.14,0.31}_{-0.05,0.06,0.07}$	$26.17^{+0.05,0.07,0.10}_{-0.05,0.06,0.07}$	$25.92^{+0.06,0.08,0.11}_{-0.07,0.11,0.16}$
		$U-V < 0.25$	$26.41^{+0.22,0.68,2.38}_{-0.10,0.14,0.16}$	$26.29^{+0.05,0.07,0.09}_{-0.05,0.06,0.07}$	$25.79^{+0.08,0.12,0.16}_{-0.09,0.14,0.21}$
		$2.5 < z \leq 3.5$	<i>B</i>	All	$26.90^{+0.16,0.37,1.00}_{-0.10,0.13,0.16}$
$J-K > 2.3$	$26.30^{+0.21,0.81,\infty}_{-0.10,0.13,0.14}$			$26.23^{+0.07,0.10,0.14}_{-0.06,0.07,0.09}$	$25.86^{+0.07,0.10,0.12}_{-0.09,0.15,0.22}$
$J-K \leq 2.3$	$26.76^{+0.24,0.74,\infty}_{-0.12,0.16,0.19}$			$26.59^{+0.05,0.07,0.09}_{-0.05,0.06,0.07}$	$26.08^{+0.07,0.09,0.11}_{-0.07,0.11,0.15}$
$U-V \geq 0.25$	$26.27^{+0.20,0.67,\infty}_{-0.09,0.12,0.13}$			$26.22^{+0.07,0.10,0.14}_{-0.06,0.07,0.09}$	$25.84^{+0.07,0.10,0.12}_{-0.09,0.15,0.23}$
$U-V < 0.25$	$26.79^{+0.25,0.93,\infty}_{-0.13,0.17,0.20}$			$26.60^{+0.05,0.07,0.09}_{-0.05,0.06,0.07}$	$26.09^{+0.07,0.09,0.11}_{-0.07,0.10,0.14}$

NOTE. — The luminosity densities are in units of $\text{erg s}^{-1} \text{Hz}^{-1} \text{Mpc}^{-3}$. The quoted errors correspond to the 1, 2, and 3 σ errors estimated from the maximum likelihood analysis as described in § 3.2 and include the contribution from photometric redshift uncertainties.

^a ρ_L^{last} is the luminosity density estimated by integrating the LF down to the faintest observed luminosities: $M_{R,AB}^{\text{last}} = -19.6$, $M_{V,AB}^{\text{last}} = -20.3$ and $M_{B,AB}^{\text{last}} = -19.5$, $M_{B,AB}^{\text{last}} = -20.0$ for the low- and high-redshift intervals, respectively; they correspond to observed K_s band magnitude of $K_s^{\text{tot}} \approx 23.14$ at the lower limit of the targeted redshift intervals.

^b ρ_L^{MUSYC} is the luminosity density estimated by integrating the LF down to the rest-frame magnitude limits of the deep NIR MUSYC survey: $M_{R,AB}^{\text{MUSYC}} = -21.8$, $M_{V,AB}^{\text{MUSYC}} = -22.4$ and $M_{B,AB}^{\text{MUSYC}} = -21.7$, -22.2 for the low- and high-redshift intervals, respectively (corresponding to observed $K_s^{\text{tot}} \approx 21.09$).

We can also compare our estimated luminosity densities in the rest-frame *B* and *V* bands with those from Rudnick et al. (2006), who presented the evolution of the rest-frame optical luminosity and stellar mass densities at $z < 3$. The luminosity density in Rudnick et al. (2006) was computed by simply adding up the luminosities of all galaxies in the targeted redshift bins with rest-frame *V*-band luminosities $> 3 \times 10^{10} L_\odot$. If we integrate our measured LF down to the same limit adopted in Rudnick et al. (2006), we obtain $\log \rho_L = 26.85 \pm 0.06$ and 26.66 ± 0.06 for the *V* and *B* band, respectively, at $z \sim 3$, and 26.48 ± 0.06 for the *B* band at $z \sim 2.2$ (units in $\text{erg s}^{-1} \text{Hz}^{-1} \text{Mpc}^{-3}$), in excellent agreement with their estimates (26.79 ± 0.05 , 26.66 ± 0.05 , and 26.37 ± 0.04 , respectively).

In § 4.2 we showed that the contribution of DRGs and red galaxies to the global LF is comparable to (or larger than) that of non-DRGs and blue galaxies at the bright end, but it becomes significant smaller at the faint end, where non-DRGs and blue galaxies dominate the global LF. In § 5.1, the contribution of DRGs to the global number density has been shown to be 13%-25% down to the faintest probed rest-frame luminosities. The contribution of DRGs to the global luminosity density is 19%-29% depending on the considered rest-frame band and redshift interval (see Table 7). Their contribution increases up to 31%-44% if we cut the composite sample to the rest-frame absolute brightness limit of MUSYC

($\sim 0.45L^*$, $0.7L^*$, $0.8L^*$ of the global LF in the rest-frame *R*, *V*, and *B* band, respectively), which reflects the increasing importance of DRGs at the bright end. A similar result holds if we consider the red galaxy subsample. Their contribution to the global luminosity density is 29%-52% down to the faintest observed luminosities and increases up to 36%-69% if we limit the analysis to the MUSYC brightness limits. From Table 7 we conclude that the total luminosity density is dominated by non-DRGs/blue galaxies, especially in the bluer rest-frame optical bands, although DRGs/red galaxies contribute about 50% at the bright end.

5.3. Stellar Mass Density Estimates

Although non-DRGs and blue galaxies represent the major contribution to the total luminosity and number densities in the rest-frame optical bands, it has been shown that DRGs usually have larger mass-to-light ratios than non-DRGs (e.g., Förster Schreiber et al. 2004; Labbé et al. 2005; van Dokkum et al. 2004), as is generally true for red versus blue galaxies (e.g., Bell & de Jong 2001; Kauffmann et al. 2003). It is therefore interesting to quantify the contribution of DRGs (red galaxies) to the total stellar mass density.

Following the method described in Rudnick et al. (2003), we estimated the stellar mass density from the measured global luminosity density modulo the mass-to-light ratio M/L . For each subsample we have measured the median rest-

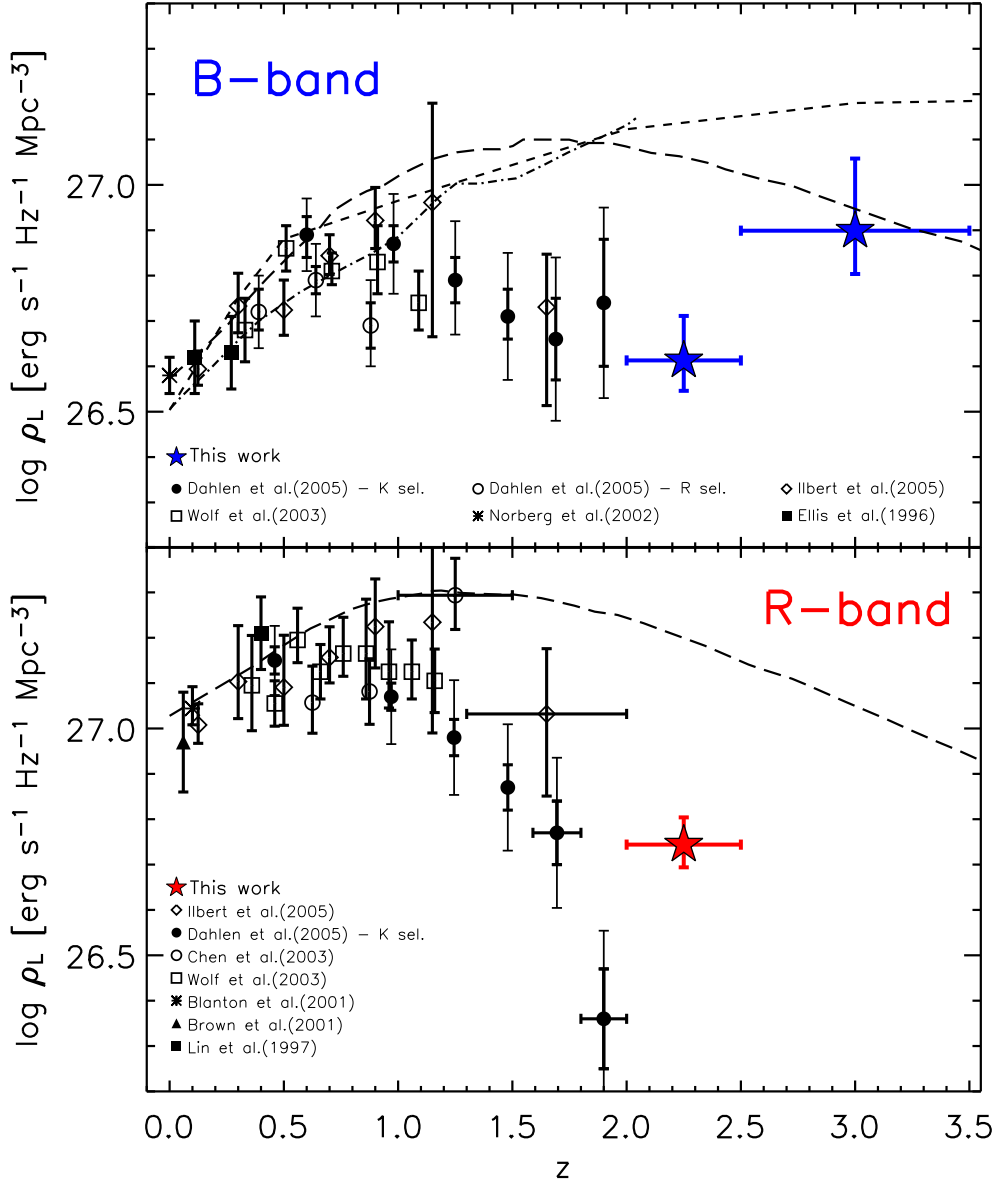


FIG. 8.— *Top*: Total rest-frame B -band luminosity density ρ_L plotted vs. the redshift. Blue filled stars are the values from this work (the error bars include also the contribution from photometric redshift uncertainties); thick error bars represent statistical errors only, while thin error bars also include the sample variance contribution to the error budget. The $z < 2$ points are taken from the 2dFGRS (Norberg et al. 2002; *asterisks*), Autofib Redshift Survey (Ellis et al. 1996; *filled squares*), COMBO-17 (Wolf et al. 2003; *open squares*), VIMOS-VLT Deep Survey (Ilbert et al. 2005; *open diamonds*), and GOODS-CDFS (Dahlen et al. 2005; R - and K -selected catalog as open and filled circles, respectively). The long- and short-dashed lines correspond to the computed B -band rest-frame luminosity densities as a function of redshift using large-scale Λ CDM hydrodynamical simulations from Nagamine et al. (2000) and Nagamine et al. (2001), respectively; the dot-dashed line is a prediction from a semianalytical model taken from Fig. 13 of Dahlen et al. (2005). *Bottom*: Total rest-frame R -band luminosity density ρ_L plotted vs. the redshift. The red filled star represents the value from this work. The $z < 2$ points are taken from the CNOC1 Redshift Survey (Lin et al. 1997; *filled squares*), Century Survey (Brown et al. 2001; *filled triangle*), SDSS (Blanton et al. 2001; *asterisk*), COMBO-17 (Wolf et al. 2003; *open squares*), Las Campanas Infrared Survey (Chen et al. 2003; *open circles*), GOODS-CDFS (Dahlen et al. 2005; *filled circles*), and VIMOS-VLT Deep Survey (Ilbert et al. 2005; *open diamonds*). The long-dashed line corresponds to the computed R -band rest-frame luminosity density as a function of redshift using large-scale Λ CDM hydrodynamical simulations from Nagamine et al. (2000).

frame $U - V$ color¹⁰, estimated the corresponding M/L ratio from the relation between $U - V$ color and M/L ratio obtained from stellar population synthesis models, and multiplied the estimated M/L ratio by the measured luminosity density to obtain the stellar mass density.

¹⁰ Rather than the median $U - V$ color of the sample, Rudnick et al. (2003) computed the global $U - V$ color from the relation: $U - V = -2.5 \log j_U + M_{\odot,U} + 2.5 \log j_V - M_{\odot,V}$, where j_U and j_V are computed by adding the luminosities of the individual galaxies. The two methods return very similar values for the $U - V$ colors.

To convert between the measured rest-frame $U - V$ color and the mass-to-light ratio M/L , we have generated stellar population synthesis models with the evolutionary synthesis code developed by G. Bruzual and S. Charlot (Bruzual & Charlot 2003). We selected the “Padova 1994” evolutionary tracks, which are preferred by Bruzual & Charlot over the more recent “Padova 2000” tracks because the latter may be less reliable and predict a hotter red giant branch leading to worse agreement with observed galaxy colors. We used the solar metallicity set of tracks. The metallicities of the

TABLE 7
DRGs/RED GALAXIES CONTRIBUTION TO THE GLOBAL LUMINOSITY AND STELLAR MASS DENSITIES

Redshift	Rest-frame Band	Sample	^a f_{ρ_L}			^b f_{ρ_*}		
$2.0 \leq z \leq 2.5$	<i>R</i>	$J-K > 2.3$	$0.27^{+0.04}_{-0.05}$	$0.29^{+0.03}_{-0.03}$	$0.41^{+0.05}_{-0.05}$	$0.62^{+0.22}_{-0.32}$	$0.66^{+0.20}_{-0.27}$	$0.67^{+0.20}_{-0.29}$
		$U-V \geq 0.25$	$0.49^{+0.06}_{-0.11}$	$0.52^{+0.04}_{-0.04}$	$0.69^{+0.04}_{-0.05}$	$0.84^{+0.10}_{-0.25}$	$0.87^{+0.07}_{-0.16}$	$0.92^{+0.05}_{-0.13}$
$2.7 \leq z \leq 3.3$	<i>V</i>	$J-K > 2.3$	$0.29^{+0.06}_{-0.05}$	$0.33^{+0.04}_{-0.03}$	$0.44^{+0.06}_{-0.05}$	$0.69^{+0.18}_{-0.28}$	$0.73^{+0.15}_{-0.23}$	$0.79^{+0.13}_{-0.22}$
		$U-V \geq 0.25$	$0.27^{+0.04}_{-0.06}$	$0.31^{+0.04}_{-0.04}$	$0.44^{+0.06}_{-0.05}$	$0.65^{+0.20}_{-0.30}$	$0.69^{+0.17}_{-0.25}$	$0.79^{+0.13}_{-0.25}$
$2.0 \leq z \leq 2.5$	<i>B</i>	$J-K > 2.3$	$0.19^{+0.05}_{-0.05}$	$0.22^{+0.03}_{-0.03}$	$0.31^{+0.06}_{-0.05}$	$0.62^{+0.26}_{-0.30}$	$0.67^{+0.21}_{-0.31}$	$0.74^{+0.20}_{-0.39}$
		$U-V \geq 0.25$	$0.37^{+0.07}_{-0.11}$	$0.43^{+0.04}_{-0.04}$	$0.58^{+0.06}_{-0.07}$	$0.87^{+0.10}_{-0.34}$	$0.89^{+0.08}_{-0.21}$	$0.90^{+0.07}_{-0.19}$
$2.5 < z \leq 3.5$	<i>B</i>	$J-K > 2.3$	$0.26^{+0.12}_{-0.10}$	$0.30^{+0.05}_{-0.03}$	$0.38^{+0.05}_{-0.06}$	$0.78^{+0.18}_{-0.43}$	$0.82^{+0.13}_{-0.28}$	$0.85^{+0.11}_{-0.31}$
		$U-V \geq 0.25$	$0.23^{+0.12}_{-0.09}$	$0.29^{+0.05}_{-0.03}$	$0.36^{+0.06}_{-0.06}$	$0.76^{+0.19}_{-0.43}$	$0.81^{+0.14}_{-0.28}$	$0.84^{+0.12}_{-0.32}$

NOTE. — The quoted errors correspond to the 1σ errors.

^a f_{ρ_L} is the contribution of DRGs/red galaxies to the global luminosity density; the three values correspond to the luminosity limits down to which the LF has been integrated: no limit, last observed point, and deep NIR MUSYC limit, respectively; see footnote of Table 6 for the specific integration limits.

^b f_{ρ_*} is the contribution of DRGs/red galaxies to the global stellar mass density as estimated in § 5.3; the three values correspond to the luminosity limits down to which the LF has been integrated to estimate the luminosity density.

DRGs are poorly known, with evidence for solar and super-solar metallicities for luminous DRGs (van Dokkum et al. 2004). These DRGs appear more metal-rich than the five LBGs at $z \sim 3$ studied by Pettini et al. (2001, $0.1-0.5 Z_{\odot}$) and similar to the seven UV-selected star-forming “BX/MD” objects at $z \sim 2$ for which Shapley et al. (2004) inferred solar, and possibly supersolar, metallicities. In all cases, however, the determinations rely on limited samples and suffer from large uncertainties. As shown by Förster Schreiber et al. (2004) adopting subsolar metallicity ($Z = 0.2Z_{\odot}$), the estimated M/L ratios are systematically lower by a factor of ≈ 2 on average. Therefore, if non-DRGs (or blue galaxies) are characterized by lower metallicities with respect to DRGs (red galaxies), the differences in M/L (and stellar mass densities) would be even larger than what is estimated assuming solar metallicities for both subsamples. For the star formation history (SFH) we used three different prescriptions: a constant star formation history (CSF model), an exponentially declining in time SFH characterized by the parameter τ (tau-model), and an instantaneous burst model (SSP model). Several values of τ were used, from $\tau = 0.1$ Gyr (the resulting model being similar to the SSP model) to 6 Gyr (closer to the CSF model). We adopted the Chabrier (2003) IMF with lower and upper IMF mass cutoffs $m_L = 0.1 M_{\odot}$ and $m_U = 100 M_{\odot}$, respectively. Adopting a different IMF would result in different derived mass-to-light ratios, which strongly depend on the shape and cutoff of the low-mass IMF (for example, assuming a Salpeter [1955] IMF, the estimated M/L ratio would be systematically larger by a factor of ~ 1.7). However, since we are interested only in the relative contribution of DRGs (red galaxies) to the global stellar mass density, the results do not depend on the adopted IMF as long as all galaxies are characterized by the same IMF. We assumed that the interstellar extinction by dust within the objects followed the attenuation law of Calzetti et al. (2000) derived empirically from observations of local UV-bright starburst galaxies under the formalism of a foreground screen of obscuring dust.

We plot in Figure 9 the relation between the rest-frame $U-V$ color and the mass-to-light ratio in the rest-frame R band, M/L_R , for the generated model tracks in the two cases with no extinction and with $A_V = 1$. It is seen that dust extinction moves the tracks roughly parallel to the model tracks. As emphasized by Bell & de Jong (2001), dust is a second-order effect for estimating stellar M/L ratios. Dust extinguishes

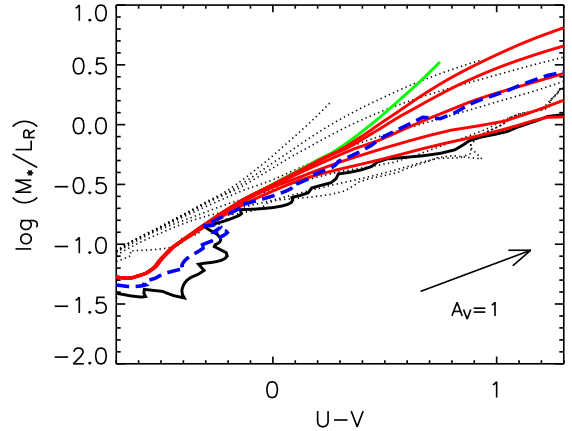


FIG. 9.— Relation between the rest-frame $U-V$ color and the mass-to-light ratio in the rest-frame R band, M/L_R , for the model tracks described in § 5.3. The dotted lines are for models with $A_V = 0$, while the other tracks are for $A_V = 1$. From top to bottom, the solid lines correspond to the CSF model (green), the tau-models ($\tau = 6, 3, 1, 0.3, 0.1$ Gyr) (red), and the SSP model (black). The blue dashed line, used in § 5.3 to estimate the contribution of DRGs and red galaxies to the total stellar mass density, corresponds to the median value of the tracks with $A_V = 1$. The arrow indicates the vector used to redden the $A_V = 0$ model to $A_V = 1$ model.

light from the stellar population, making it dimmer; however, dust also reddens the stellar population, making it appear to have a somewhat larger stellar M/L ratio. To first order, these effects cancel out, leaving a dust-reddened galaxy on the same color–stellar M/L ratio correlation.

Using the relation between color and M/L , we convert the estimated median rest-frame $U-V$ color and the measurements of the luminosity densities ρ_L to stellar mass density estimates ρ_* . Specifically, we adopted the median value of M/L within the family of considered model tracks with $A_V = 1$ (blue dashed line plotted in Figure 9 for the rest-frame R band); the error on the M/L was chosen as half of the difference between the upper and lower envelope of the model tracks. The median rest-frame $U-V$ color of each subsample and the corresponding M/L in the rest-frame B , V , and R bands are listed in Table 8.

Although the values of the stellar mass densities of the individual subsamples might be affected by very large uncertainties, the relative contribution to the global stellar mass density of DRGs (red galaxies) and non-DRGs (blue galaxies) should be more robust. The contribution f_{ρ_*} of the DRGs (red galax-

TABLE 8
REST-FRAME $U-V$ COLORS AND ESTIMATED M/L RATIOS

Redshift	Rest-Frame Band	Sample	^a $U-V$	^b $\log M/L$
$2.0 \leq z \leq 2.5$	<i>R</i>	$J-K > 2.3$	0.66 (0.67)	0.05 ± 0.32 (0.06 ± 0.32)
		$J-K \leq 2.3$	-0.06 (0.19)	-0.63 ± 0.07 (-0.41 ± 0.10)
		$U-V \geq 0.25$	0.60 (0.62)	-0.00 ± 0.27 (0.01 ± 0.28)
		$U-V < 0.25$	-0.23 (-0.13)	-0.78 ± 0.04 (-0.71 ± 0.09)
$2.7 \leq z \leq 3.3$	<i>V</i>	$J-K > 2.3$	0.57 (0.57)	-0.08 ± 0.28 (-0.08 ± 0.28)
		$J-K \leq 2.3$	-0.19 (-0.14)	-0.80 ± 0.05 (-0.75 ± 0.05)
		$U-V \geq 0.25$	0.59 (0.57)	-0.05 ± 0.30 (-0.08 ± 0.28)
		$U-V < 0.25$	-0.18 (-0.14)	-0.75 ± 0.05 (-0.75 ± 0.05)
$2.0 \leq z \leq 2.5$	<i>B</i>	$J-K > 2.3$	0.66 (0.67)	0.00 ± 0.40 (0.00 ± 0.40)
		$J-K \leq 2.3$	-0.06 (0.19)	-0.85 ± 0.05 (-0.60 ± 0.15)
		$U-V \geq 0.25$	0.60 (0.62)	-0.10 ± 0.35 (-0.05 ± 0.35)
		$U-V < 0.25$	-0.23 (-0.13)	-1.15 ± 0.15 (-0.85 ± 0.05)
$2.5 < z \leq 3.5$	<i>B</i>	$J-K > 2.3$	0.56 (0.56)	-0.13 ± 0.33 (-0.13 ± 0.33)
		$J-K \leq 2.3$	-0.26 (-0.20)	-1.15 ± 0.15 (-1.10 ± 0.20)
		$U-V \geq 0.25$	0.57 (0.57)	-0.13 ± 0.33 (-0.13 ± 0.33)
		$U-V < 0.25$	-0.25 (-0.20)	-1.15 ± 0.15 (-1.10 ± 0.20)

^aMedian rest-frame $U-V$ color of the considered subsample; the numbers in parentheses correspond to the median $U-V$ colors of the subsamples brighter than the MUSYC magnitude limit.

^b $\log M/L$ is the logarithm of the mass-to-light ratio in solar units assuming $A_V = 1$ mag, calculated as described in § 5.3; the numbers in parentheses correspond to the mass-to-light ratios of the samples brighter than the MUSYC magnitude limit.

ies) to the global stellar mass density is listed in Table 7.

Adopting the same assumptions for the stellar population synthesis models of DRGs (red galaxies) and non-DRGs (blue galaxies) (i.e., the median value of the considered model track), we see from Table 8 that DRGs (red galaxies) have M/L ratios systematically higher than non-DRGs (blue galaxies) by a factor of ~ 5 -11 depending on the rest-frame band (higher in the bluer bands). The differences in M/L are smaller when the brighter samples (down to the MUSYC limit) are considered, with the M/L of DRGs (red galaxies) being a factor of ~ 3 -9 (4-9) larger with respect to non-DRGs (blue galaxies). For comparison, from the analysis of *Spitzer*-IRAC imaging on HDF-S, Labbé et al. (2005) found that the average mass-to-light ratio of DRGs in the rest-frame *K* band is about a factor of ~ 3 larger than LBGs, finding a correlation between M/L_K and rest-frame $U-V$ color. Consistently, from SED modeling of the $2 \leq z \leq 3.5$ FIRES galaxies, Förster Schreiber et al. (2004) found that the median rest-frame *V*-band M/L of DRGs is ~ 1.2 -2.3 $M_\odot L_{V,\odot}^{-1}$ (~ 0.4 for LBGs). The higher values of M/L for DRGs agree very well also with the results from SED fitting of individual galaxies in van Dokkum et al. (2004), who found for DRGs a median value $M/L_V \approx 0.8$ (M/L) $_\odot$. Finally, our estimated M/L_V are in excellent agreement with those estimated in Rudnick et al. (2006).

Because of the systematically larger mass-to-light ratios, DRGs (red galaxies) dominate the global stellar mass density, with contributions in the range 66%-82% (69%-89%) down to the faintest probed rest-frame luminosities. The contribution of DRGs (red galaxies) increases up to 67%-85% (79%-92%) if the brightest sample is considered (down to the rest-frame magnitude limits of the deep NIR MUSYC). These numbers are consistent with the results of van Dokkum et al. (2006). From a complete mass-selected sample ($M_* > 10^{11} M_\odot$) constructed with MUSYC, FIRES, and GOODS-CDFS, they estimated that DRGs in the redshift interval $2 < z < 3$ make up 77% of the total stellar mass, in very good agreement with our results. Our results are in qualitative good agreement also with the results from Rudnick et al. (2006), who found that the DRGs contribute 64% of the stellar mass density at $z \sim 2.8$

and 30%-50% at $z \sim 2$.

We stress that the estimated contributions of DRGs and red galaxies to the global stellar mass density are very uncertain and need confirmation from detailed SED analysis of mass-limited (rather than luminosity-limited) samples.

6. SUMMARY AND CONCLUSIONS

In this paper we have measured the rest-frame optical (*R*, *V*, and *B* band) luminosity functions of galaxies at redshifts $2 \leq z \leq 3.5$ from a composite sample constructed with the deep NIR MUSYC, the ultra-deep FIRES, and the GOODS-CDFS. The large surveyed area (~ 378 arcmin², 76% of which comes from the deep NIR MUSYC) of the composite sample and the large range of luminosities spanned allows us to measure the bright end of the LF and to constrain the faint-end slope. Moreover, the several independent fields and their large area enabled us to largely reduce uncertainties due to sample variance, especially at the bright end. We have used Monte Carlo simulations to show that the uncertainties in the photometric redshift estimates do not significantly affect the measured parameters of the LF in the studied redshift regimes. There is a hint for a steepening in the faint-end slope of the LF from the rest-frame *R* band to the *B* band, although the differences are not significant. The measured LF faint-end slopes at $z > 2$ are consistent, within the errors, with those in the local LFs. The characteristic magnitudes are significantly brighter than the local ones (e.g., ~ 1.2 mag in the rest-frame *R* band), while the measured values for Φ^* are typically a factor of ~ 5 smaller with respect to the local values.

The large number of objects in the composite sample allowed the first measurement of the LF of DRGs (defined based on their observed $J-K$ color), which we compared to that of non-DRGs in the same redshift range. The DRG population is characterized by a very different LF than that of non-DRGs, especially at the faint end. While at the bright end the LF of DRGs is similar to that non-DRGs, at the faint end the latter one has a significantly steeper faint-end slope, especially in the rest-frame *R* band. The significance of the difference between the LFs of DRGs and non-DRGs decreases going to bluer rest-frame bands and to higher redshifts, although this is mainly caused by decreasing constraints on the

faint end of the LF of DRGs. Qualitatively similar results are found if we compare the LFs of red (rest-frame $U-V \geq 0.25$) and blue (rest-frame $U-V < 0.25$) galaxies in the same redshift intervals, with the former equally contributing (or even dominating) at the bright end and the latter dominating the faint end.

In the rest-frame V band we have also compared the LFs of blue galaxies (non-DRGs) with those of LBGs in the same redshift range. Although the two LFs agree very well at the bright end, the faint-end slope estimated by Shapley et al. (2001) is much steeper than the one measured in this paper. As the rest-frame optical LF of LBGs was estimated in Shapley et al. (2001) from the rest-frame UV LF and the observed distribution of \mathcal{R} - K_s colors as a function of \mathcal{R} magnitude, their steeper slope could be a result of an overestimate of the regression slope of the correlation between \mathcal{R} - K_s and \mathcal{R} and/or of the faint-end slope of the adopted rest-frame UV LF of LBGs. Supporting the former possibility is the work of Labbé et al. (2006), who do not find any positive correlation between R magnitudes and $R-K_s$ colors in their deeper sample. Support for the latter comes from the very recent work of Sawicki & Thompson (2006), who measured the rest-frame UV LF for $z \sim 3$ LBGs from the Keck Deep Fields (KDF; Sawicki & Thompson 2005) and find a faint-end slope $\alpha = -1.43^{+0.17}_{-0.09}$, significantly shallower than the one adopted in Shapley et al. (2001). Alternatively, our blue K_s -selected (i.e., rest-frame optical selected) galaxies might simply constitute a different population than the $z \sim 3$ LBGs (rest-frame UV selected), with different characterizations of the LF at the faint end. We also caution that our measurements of the faint-end slopes still have significant uncertainties due to small number statistics.

We generally find good agreement between our measured rest-frame B -band LFs at $2.5 < z \leq 3.5$ and those previously published by Poli et al. (2003), Giallongo et al. (2005), and Gabasch et al. (2004). In the redshift range $2 \leq z \leq 2.5$, the agreement between our rest-frame B - and R -band LFs and those measured by Gabasch et al. (2004, 2006) from the FDF survey is less good, especially for the R band. Their Schechter parameters α and M^* are consistent with ours only at the 2σ level in the rest-frame R band, while their estimated Φ^* is larger than ours by a factor of ~ 1.3 - 1.6 in the rest-frame B and R band, respectively. We have shown that this disagreement may be due to the spectroscopically confirmed existence of a (proto)cluster at $z = 2.35$ in the single field FDF survey.

From the measured LFs we have estimated the number and luminosity densities of the global population of high- z galaxies and of various subsamples. The contribution of DRGs (red galaxies) to the global number density is only $\sim 13\%$ - 25% (18% - 29%) down to the faintest probed rest-frame luminosities. However, we have shown that field-to-field variations can be very significant (up to a factor of ~ 3), especially for relatively bright samples, in accord with the highly clustered nature of high luminosity and red galaxies (Adelberger et al. 2005; Daddi et al. 2003; Quadri et al. 2007a). The contribution of DRGs (red galaxies) to the global luminosity density is $\sim 20\%$ - 30% (30% - 50%), higher in the redder rest-frame bands (which are less affected by extinction and better tracers of the underlying stellar mass) and at lower redshifts. With respect to the lower z luminosity density estimates from the literature, we confirm the trend of slowly decreasing rest-frame R -band luminosity densities beyond $z \sim 1$, with $\rho_{L,R}$ at $z \sim 2.3$ being a factor of ~ 2 smaller than the local one. In the rest-frame B band, the measured global luminosity density

at $z \sim 2.3$ is similar to the local value. At $z \sim 3$, the estimated global luminosity density may be a factor of ~ 2 higher, similar to the values around $z \sim 1$.

Finally, using stellar population synthesis models, we have derived the mass-to-light ratios of the considered subsamples by converting the estimated median rest-frame $U-V$ color into M/L . In the rest-frame R and V bands, the mass-to-light ratios of DRGs (red galaxies) are a factor of ~ 5 larger than non-DRGs (blue galaxies), consistent with previous works. In the rest-frame B band the difference in M/L is higher, up to a factor of ~ 11 . Using the estimated M/L , we have quantified the contribution of DRGs and red galaxies to the global stellar mass density, finding that the total stellar mass budget is dominated by DRGs (red galaxies), whose contribution is of order $\sim 60\%$ - 80% of the global value. We caution that our M/L ratios estimates are very rough and characterized by very large uncertainties and need confirmation from detailed SED analysis.

The main limitation of this work is the small number statistics at the very faint end of the LF, which is probed only by the ultra-deep FIRES. The faint-end slopes of the DRG and red galaxy subsamples are especially uncertain. To make further progress in the determination of the LF of different galaxy populations at $z > 2$ and to better constrain the global LFs, it is crucial to better probe the faint end of the LFs. This can only be achieved with ultradeep NIR imaging with high-quality optical data over many spatially disjoint fields, in order to improve the statistics at the faint end and to mitigate the effect of field-to-field variations. Although we have shown that well-behaved photometric redshift errors do not affect significantly the measurement of the LF, the heavy reliance on photometric redshifts is another limitation of this work, since ‘‘catastrophic’’ failures and systematic errors could potentially affect the LF measurements. Obtaining large numbers of spectroscopic redshifts for K -selected high- z sources has proven difficult and extremely time consuming. Even though the success rate for measuring spectroscopic redshift for bright galaxies is high with NIR spectroscopy (Kriek et al. 2006), only the use of multiobject NIR spectrographs will make it possible to construct a large sample of high- z K -selected galaxies with spectroscopic redshift measurements. Further advances can be expected from further extension of the wavelength range into the red. Scheduled *Spitzer* IRAC observations on the deep NIR MUSYC fields will allow us to (1) separate old and passively evolving galaxies from heavily obscured and strongly active star-forming galaxies (see Labbé et al. 2005), making it possible to study the LF of physically different types of galaxies; (2) extend the robust measurement of the LF at redshift $2 < z < 3$ into the rest-frame NIR, which is much closer to a selection by stellar mass; (3) convert the measured rest-frame NIR luminosity function into a mass function and study the evolution of the stellar mass density; and (4) extend the study of the rest-frame optical LFs to even higher redshifts.

We thank all the members of the MUSYC collaboration for their contribution to this research. MUSYC has greatly benefited from the support of Fundación Andes and the Yale Astronomy Department. D.M. is supported by NASA LTSA NNG04GE12G. The authors acknowledge support from NSF CARRER AST-0449678. E.G. is supported by NSF Fellowship AST-0201667. P.L. is supported by Fondecyt Grant #1040719. We thank the anonymous referee for comments and suggestions which helped improve the paper.

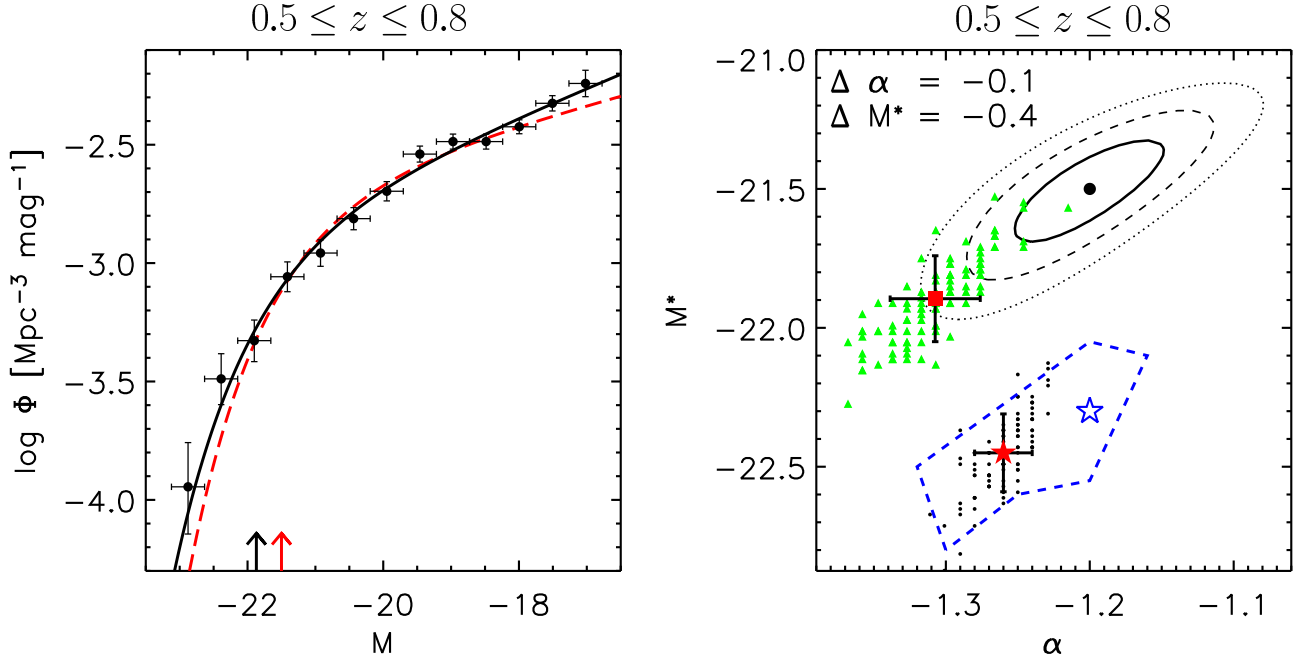


FIG. A1.— *Left*: Intrinsic Schechter LF (red dashed line) compared to the observed LF at $0.5 \leq z \leq 0.8$ corresponding to the median Monte Carlo realization (black solid line and filled circles correspond to the maximum likelihood and $1/V_{\max}$ method, respectively); the best-fit M^* are also plotted as arrows. *Right*: Measured Schechter parameters M^* plotted vs. α ; the black filled circle represents the input parameters of the “observed” model catalog, together with the 1, 2, and 3 σ contour levels; the green filled triangles represent the 100 Monte Carlo realizations; the red filled square is the median realization, and the plotted error bars represent the rms in α and M^* . The amount of the systematic effects in α and M^* are also specified. The red filled star represents the median realization when the redshifts of the objects are extracted from a random uniform distribution, as done in Chen et al. (2003); the small black filled circles represent the corresponding 100 Monte Carlo realizations. The result from Chen et al. (2003) is also shown (blue open star) together with its 99% uncertainties (blue dashed contour).

APPENDIX

APPENDIX A

EFFECTS OF UNCERTAINTIES IN Z_{PHOT} : MONTE CARLO SIMULATIONS

In order to quantify the systematic effects on the LF parameters α and M^* due to the uncertainties in the photometric redshift estimates, we performed a series of Monte Carlo simulations. First, we generated several model catalogs of 25,000 galaxies with redshifts between $z_{1,\text{MC}}$ and $z_{2,\text{MC}}$ and with luminosities drawn from an input Schechter LF. While in the Monte Carlo simulations of Chen et al. (2003) the redshifts of the objects in the mock catalogs were extracted from a random uniform distribution, we took into account the fact that, under the assumption of no evolution in the number density, the probability of a galaxy existing at the redshift z is proportional to the volume:

$$p(z) \propto \frac{dV}{dz} \propto \frac{d_L^2(z)}{(1+z)^2} \frac{1}{\sqrt{\Omega_\Lambda + \Omega_M(1+z)^3}}, \quad (\text{A1})$$

where d_L is the luminosity distance. Since in a real survey galaxies are selected down to a limiting apparent magnitude, the final mock catalogs are obtained after applying a limit in the observed apparent magnitude. The effect of a limiting apparent magnitude is that, at a fixed observed magnitude, intrinsically fainter sources are systematically excluded from the catalog at higher redshift. Next, as done by Chen et al. (2003), we assumed a redshift error function parameterized as a Gaussian distribution function of 1 σ width $\sigma'_z(1+z)$, with σ'_z the scatter in $\Delta z/(1+z_{\text{spec}})$, and we formed an observed redshift catalog by perturbing the input galaxy redshift within the redshift error function. Finally, we determined the LF for the galaxies at $z_1 \leq z \leq z_2$ using the $1/V_{\max}$ and maximum likelihood methods described in § 3. Note that we ignore K -correction in our Monte Carlo simulations.

We first studied the effects of the photometric redshift uncertainties at $z < 1$, by using $z_{1,\text{MC}} = 0.15$, $z_{2,\text{MC}} = 1.6$, and assuming an input Schechter LF with parameters $\alpha = -1.2$ and $M^* = -21.5$ (as in Chen et al. 2003). In order to compare our results with those from the Monte Carlo simulations in Chen et al. (2003), we used $\sigma'_z = 0.15$ and we measured the LF in the same redshift range $0.5 \leq z \leq 0.8$. We find that the median measured M^* is brighter than the intrinsic value by ~ 0.4 mag and that the measured α is steeper on average than the intrinsic value by ~ 0.1 . This result is shown in Figure A1: in the left panel, the input Schechter LF is compared to the median Monte Carlo realization; in the right panel, the 100 Monte Carlo realizations are plotted in the $\alpha - M^*$ plane and compared to the best-fit values and the corresponding 1, 2, and 3 σ contour levels of the LF measured on the redshift-unperturbed mock catalog.

As shown in Figure A1, the measured systematic effects on α and M^* caused by the redshift uncertainties arise from an excess of sources at both the faint and the bright end of the LF. A careful analysis of the Monte Carlo simulations reveals the origin of these excesses. Because of the uncertainties in the redshifts, sources can scatter from high to low redshifts, and vice versa. As the probability of a galaxy existing at redshift z is proportional to dV/dz (which peaks at $z \sim 2.5$), the number of sources that scatter from higher redshifts to lower ones is much larger than vice versa. This is evident in Figure A2, where the rest-frame

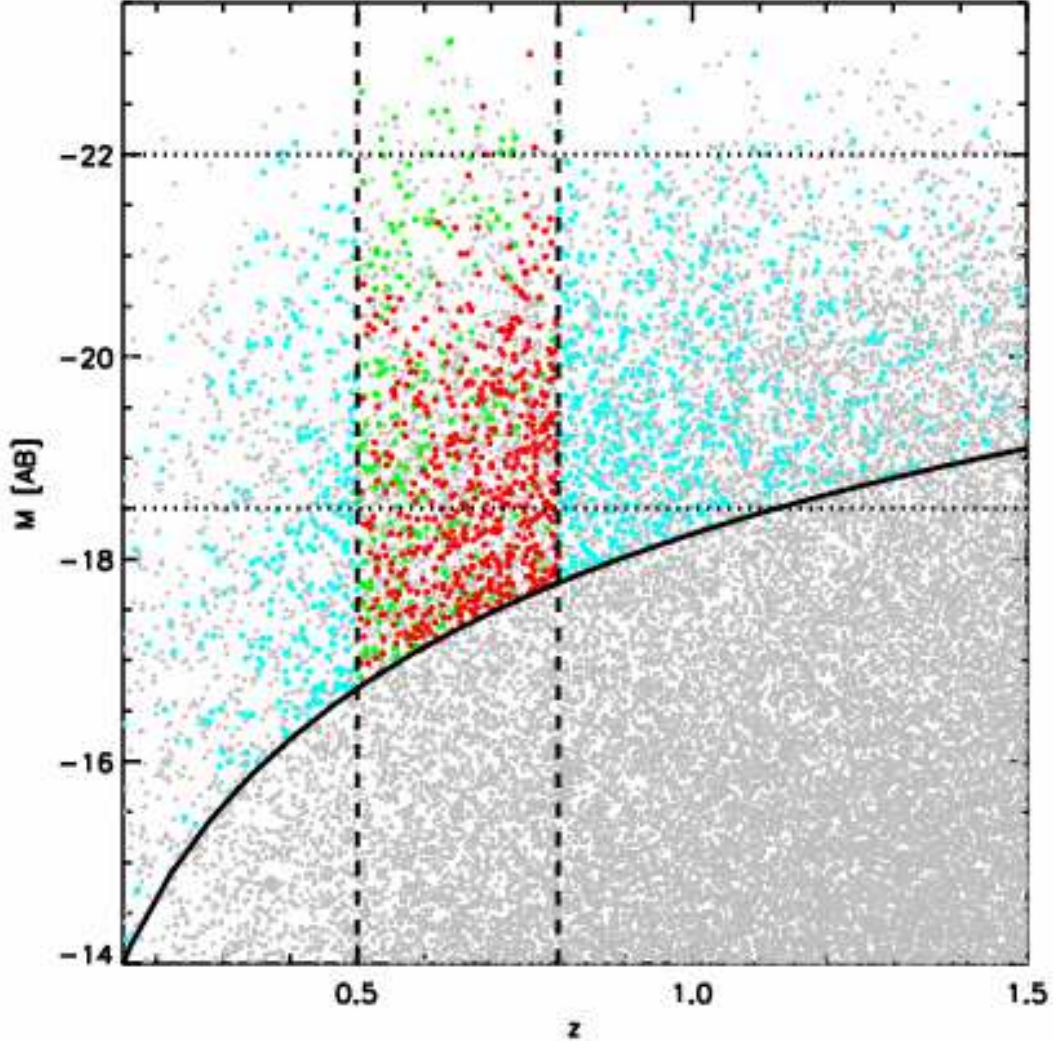


FIG. A2.— Rest-frame absolute magnitudes M plotted vs. the redshifts z of the redshift-unperturbed mock catalog (*gray points*). The solid line represents the limiting magnitude of the sample as a function of redshift; the two vertical dashed lines represent the redshift interval within which the LF is measured. Cyan filled circles at $z > 0.8$ are the sources that in the redshift-perturbed mock catalog scatter from high z into the considered redshift bin (*red filled circles*); the cyan filled circles at $z < 0.5$ are the sources that scatter from low z into the considered redshift bin (*green filled circles*). The loci at magnitudes fainter than the lower dotted line and brighter than the upper dotted line are the regions where we observe the excess of sources at the faint and bright ends (evident in the left panel of Fig. A1), respectively.

absolute magnitudes of the mock catalog are plotted versus redshift: at a fixed magnitude, the number of sources is larger at higher redshifts.

Since an object in the mock catalog is characterized by a fixed apparent magnitude, a new redshift estimate translates into a new rest-frame absolute magnitude; e.g., when a source “scatters” from high to low redshift, the estimated absolute brightness is fainter than the intrinsic value, and the object moves, in Figure A2, from right to left along a line parallel to the black solid line. Moreover, at any redshift, there are more sources at faint magnitudes than at bright ones because of the shape of the LF. Therefore, the sources scattering from high redshifts into the considered redshift bin (plotted in Fig. A2 in cyan) preferentially end up at fainter magnitudes (plotted in red), producing the excess at the faint end of the LF with respect to the input LF. The excess at the bright end is instead mainly produced by those sources that scatter into the considered redshift range coming from lower redshifts (represented in Fig. A2 with cyan and green filled circles); since at the bright end the number of objects is very small, even a handful of new sources can significantly increase the measured density with respect to the intrinsic one. Because at low redshifts the dependency of dM/dz with redshift is strong, even small uncertainties in the redshift estimate have large effects on the rest-frame absolute magnitude. For example, at $z \sim 0.7$, a $\Delta z = 0.25$ results in a $\Delta M \sim 0.7 - 1$ mag (only 0.1-0.2 mag at $z = 2.25$).

The systematic effect on M^* that we derive ($\Delta M^* \sim -0.4$ mag) is about half the effect found by Chen et al. (2003). Also almost no systematic effect in α was found in their work. It seems very likely that these differences might be due to the fact that the redshifts are drawn from a random uniform distribution in Chen et al. (2003) while in our Monte Carlo simulations they are extracted from the probability function specified in Eq. A1. In the former case, there would be a much larger number of low- z sources that can scatter into the considered redshift bin, resulting in a larger excess of sources at the bright end and therefore a larger systematic effect in M^* . If we repeat our Monte Carlo simulations extracting the redshifts of the sources from a random uniform distribution, we obtain $\Delta M^* \sim -0.9$ mag and $\Delta \alpha \sim -0.06$, consistent with the result of Chen et al. (2003) as shown in

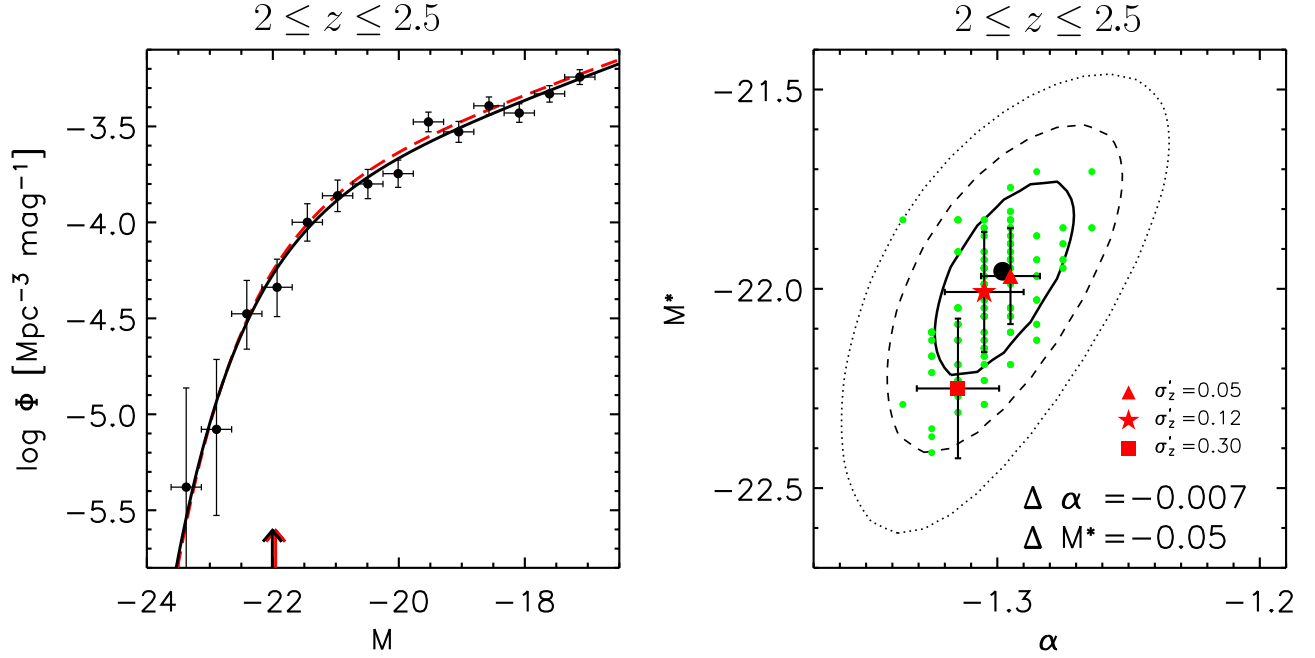


FIG. A3.— *Left*: Input Schechter LF (red dashed line) compared to the observed LF at $2 \leq z \leq 2.5$ of the median Monte Carlo realization (black solid line and filled circles correspond to the maximum likelihood and $1/V_{\max}$ methods, respectively); the best-fit M^* are also plotted as arrows. *Right*: Measured Schechter parameters M^* plotted vs. α ; the filled black circle represents the input parameters of the “observed” model catalog, together with the 1, 2, and 3 σ contour levels; small green filled circles represent the 100 Monte Carlo realizations using $\sigma'_z = 0.12$; the red filled star is the corresponding median realization; the red filled triangle and square represent the median realization of the Monte Carlo simulations with $\sigma'_z = 0.05$ and $\sigma'_z = 0.3$, respectively. The amount of the systematic effect in α and M^* is also specified for $\sigma'_z = 0.12$.

the right panel of Figure A1.

Next, we repeated our Monte Carlo simulations at higher redshift by generating model catalogs with galaxies at redshifts between $z_{1,\text{MC}} = 1$ and $z_{2,\text{MC}} = 6$, since the goal of this paper is to measure the LF of galaxies in the redshift intervals $2 \leq z \leq 2.5$ and $2.5 < z \leq 3.5$. In Figure A3 we plot the results of our Monte Carlo simulations at $2 \leq z \leq 2.5$, assuming an input Schechter LF with $\alpha = -1.3$ and $M^* = -22$ and for $\sigma'_z = 0.12$ (which corresponds to the photometric redshift errors in the deep NIR MUSYC for $z > 1.5$ objects).

The systematic effects on the measured α and M^* are now very small, $\Delta M^* = -0.05$ mag and $\Delta \alpha = -0.007$, and negligible with respect to the other uncertainties on the estimated best-fit parameters. Similar results are obtained in the redshift bin $2.5 < z \leq 3.5$. At $2 \leq z \leq 3.5$, the effect due to $p(z) \propto dV/dz$ is much smaller than at $z < 1$, since $p(z)$ peaks at $z \sim 2.5$ and then decreases very slowly, so that the number of high- and low- z sources scattering into the considered redshift bin is similar to the number of sources scattering out. Also, at $z > 2$, the error on the rest-frame absolute magnitude corresponding to a redshift error is significantly smaller than at $z < 1$; e.g., $\Delta M = 0.3 - 0.4$ mag for $\Delta z \sim 0.4$ at $z = 2.25$. Therefore, the measured LF is similar to the input one and the systematic effects on α and M^* are negligible compared to the uncertainties in the LF estimates for reasonable values of σ'_z ($\lesssim 0.12$).

We repeated the above Monte Carlo simulations assuming different input α (-1.5 , -1 , and -0.5) to study the behavior of the systematic effects as function of the faint-end slope. No significant differences are found: $-0.04 < \Delta M^* < 0.01$ mag for $\alpha = -1$ and -0.5 (depending on the considered redshift bin); for $\alpha = -1.5$, the systematic effect is slightly larger ($\Delta M^* \sim -0.07 / +0.08$ mag for $2 \leq z \leq 2.5$ and $2.5 < z \leq 3.5$, respectively), but also the uncertainties on the best-fit M^* increase with steeper faint-end slopes (since the observed LF appears more like a power law) so that the systematic effects on the measured best-fit Schechter parameters remain very small with respect to the uncertainties on the best-fit values.

Finally, we investigated the effects of non-Gaussian redshift error probability distributions. First, using a model catalog with galaxies at redshifts between $z_{1,\text{MC}} = 0.1$ and $z_{2,\text{MC}} = 6$, we simulated the effect of a 5% “catastrophic” outliers by assigning random redshifts to 5% of the mock catalog. Adopting the input LF with $\alpha = -1.3$ and $M^* = -22.0$ and assuming $\sigma'_z = 0.12$, we find larger systematic effect in both α and M^* by a factor of almost 2. Next, we built the mean redshift probability distribution of the deep NIR MUSYC by averaging the individual redshift probability distribution for each galaxy calculated by the used photometric redshift code (for details see Rudnick et al. 2003). The average MUSYC redshift probability distribution is well modeled by a Lorentzian function, rather than a Gaussian function. We find a larger systematic effect in α , twice as much as the corresponding effect assuming a Gaussian parametrization for the redshift probability distribution, but similar systematic effect in M^* , although in the opposite direction. To summarize, although the systematic effects in α and M^* expectedly get larger when we simulate “catastrophic” outliers or we adopt a redshift error function with broader wings compared to the Gaussian model, they remain much smaller than the random uncertainties in the LF estimates.

We also quantified the systematic effect on the luminosity density estimates. We find that the effect is of the order of a few percent (always $< 6\%$) depending on the considered redshift interval and on the input Schechter LF.

In order to include this contribution in the error budget, we conservatively assume a 10% error contribution to the luminosity density error budget due to uncertainties in the photometric redshift estimates.

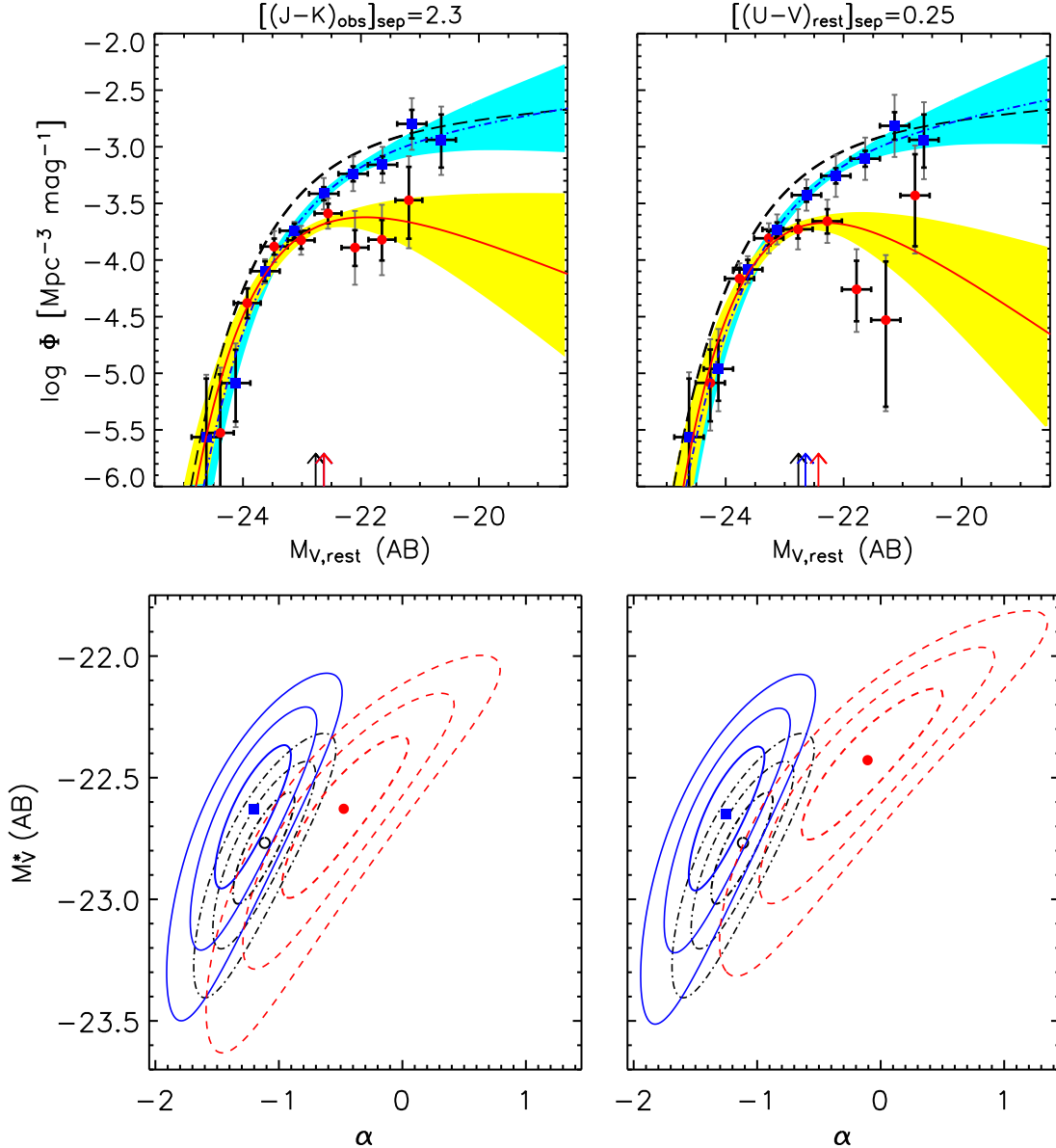


FIG. B1.— Rest-frame V-band LF at $2.7 \leq z \leq 3.3$. *Top*: Rest-frame V-band LFs at $2.7 \leq z \leq 3.3$ for DRGs/non-DRGs (*left*) and red/blue galaxies (*right*). The red solid line and filled circles represent the LF of DRGs and red galaxies estimated with the STY and $1/V_{\max}$ methods, respectively; the blue dot-dashed line and filled squares represent the LF of non-DRGs and blue galaxies. The rest-frame V band LF of all galaxies is also plotted (*black dashed line*). The shaded regions represent the 1σ uncertainties of the LFs measured with the STY method. The arrows represent the best-fit M_V^* ; error bars as in Fig. 5. *Bottom*: 1 , 2 , and 3σ contour levels from the STY method for DRGs and red galaxies (*red dashed lines*), for non-DRGs and blue galaxies (*blue solid lines*), and for all galaxies (*black dot-dashed lines*); the best-fit Schechter values are also plotted (red filled circle for DRGs and red galaxies, blue filled square for non-DRGs and blue galaxies, and open circle for all galaxies).

APPENDIX B

REST-FRAME V- AND B-BAND LUMINOSITY FUNCTIONS FOR DRGS/NON-DRGS AND RED/BLUE GALAXIES

In the body of the paper we showed the rest-frame R band LFs of DRGs, non-DRGs, red and blue galaxies (see Fig. 5). For completeness, we show here the comparison of the LFs of DRGs (red galaxies) and non-DRGs (blue galaxies) discussed in § 4.2 in the rest-frame V band at $2.7 \leq z \leq 3.3$ (Fig. B1) and in the rest-frame B band at $2 \leq z \leq 2.5$ (Fig. B2) and at $2.5 < z \leq 3.5$ (Fig. B3). The corresponding best-fit Schechter parameters are listed in Table 3.

APPENDIX C

COMPARISON WITH PREVIOUSLY PUBLISHED LUMINOSITY FUNCTIONS

Here we compare our results to previous rest-frame optical LF studies at $z > 2$, which were based on smaller samples. We note that these studies are affected by significant uncertainties due to field-to-field variance (as they are based on a single field or on a very small total surveyed area) and by small number statistics at the bright end.

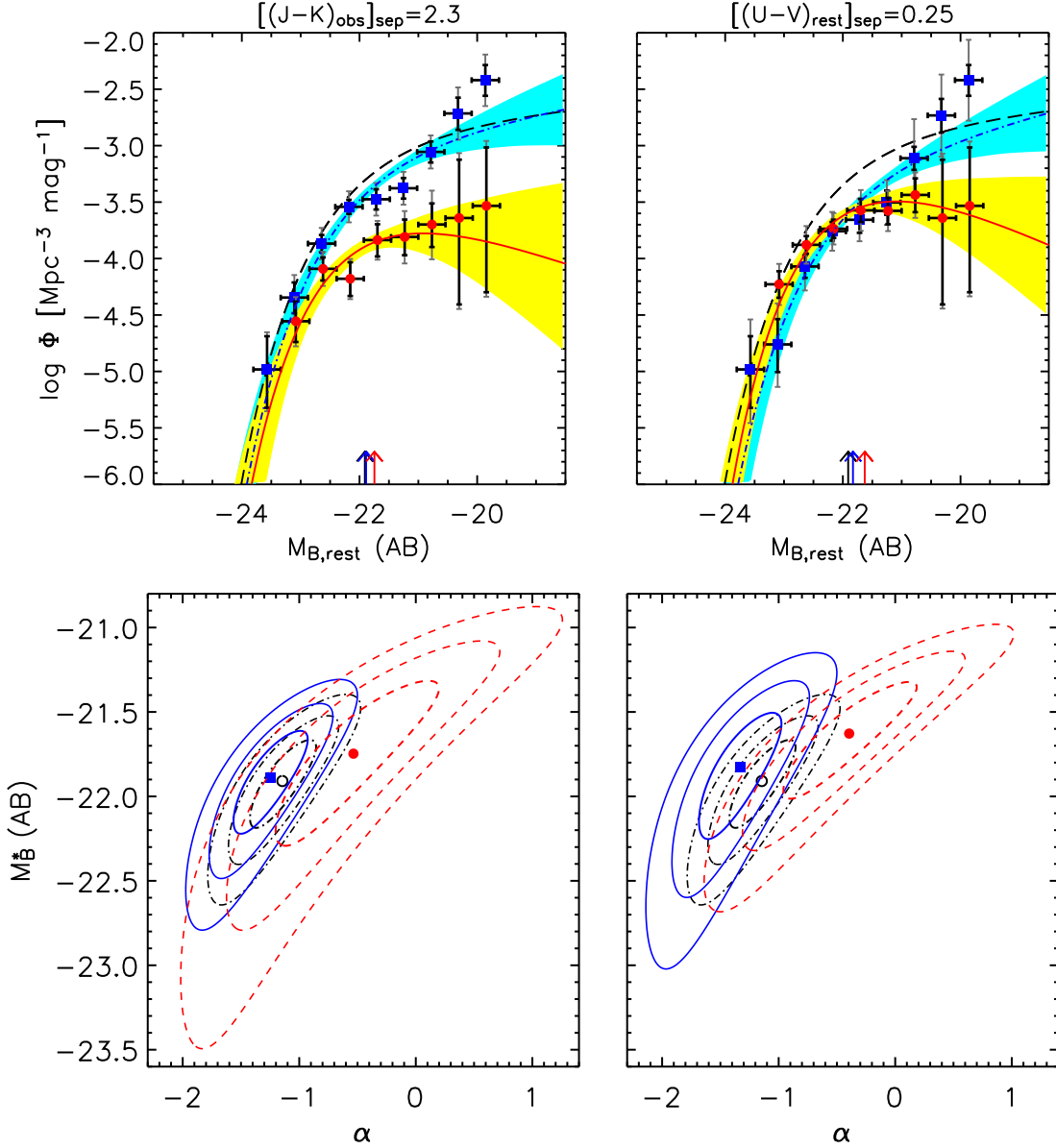


FIG. B2.— Rest-frame B-band LF at $2 \leq z \leq 2.5$; symbols as in Fig. B1.

C1. POLI ET AL. (2003) AND GIALLONGO ET AL. (2005)

Poli et al. (2003) analyzed a sample of 138 K -selected galaxies down to $K_{AB} = 25$ to construct the rest-frame B -band LF in the redshift range $1.3 < z < 3.5$. The total area of their composite sample is ~ 68 arcmin², a factor of ~ 5.6 smaller than the area sampled in this work. Giallongo et al. (2005) repeated the analysis in Poli et al. (2003) with an improved composite sample (although with the same area) and allowing the Schechter parameters Φ^* and M^* to vary with the redshift, while α is kept constant at the low-redshift value ($z < 1$). A direct comparison between the LFs of Poli et al. (2003) and Giallongo et al. (2005) and the LF measured in this work is shown in Figure C1 (*left panel*) for the redshift range $2.5 < z \leq 3.5$.

First, we note in Figure C1 how much better the bright end of the LF is constrained from our work: the large area of the composite sample ($\sim 76\%$ of which comes from the deep NIR MUSYC alone) allows us to sample the LF up to B -band magnitudes ~ 1.5 mag brighter than done in Poli et al. (2003) and Giallongo et al. (2005). Our measurements of the LF using the $1/V_{\max}$ method are consistent within the errors with those in both Poli et al. (2003) and Giallongo et al. (2005). The best-fit LF estimated with the maximum likelihood analysis in Poli et al. (2003) is consistent, within the errors, with our best-fit solution. However, the best-fit LF estimated with the maximum likelihood analysis in Giallongo et al. (2005) is significantly different from ours, as clearly shown in the inset of Figure C1 (*left panel*). While their faint-end slope is consistent with our best-fit α , their lack of constraints on the bright end of the LF results in a much fainter M_B^* (by ~ 0.6 mag).

C2. GABASCH ET AL. (2004, 2006)

Gabasch et al. (2004, 2006) analyzed a sample of 5558 I -selected galaxies down to $I_{AB} = 26.8$ (50% completeness limit) from the FDF survey (Heidt et al. 2003) to study the evolution of the rest-frame B - and r -band LF over the redshift range $0.5 < z < 5$.

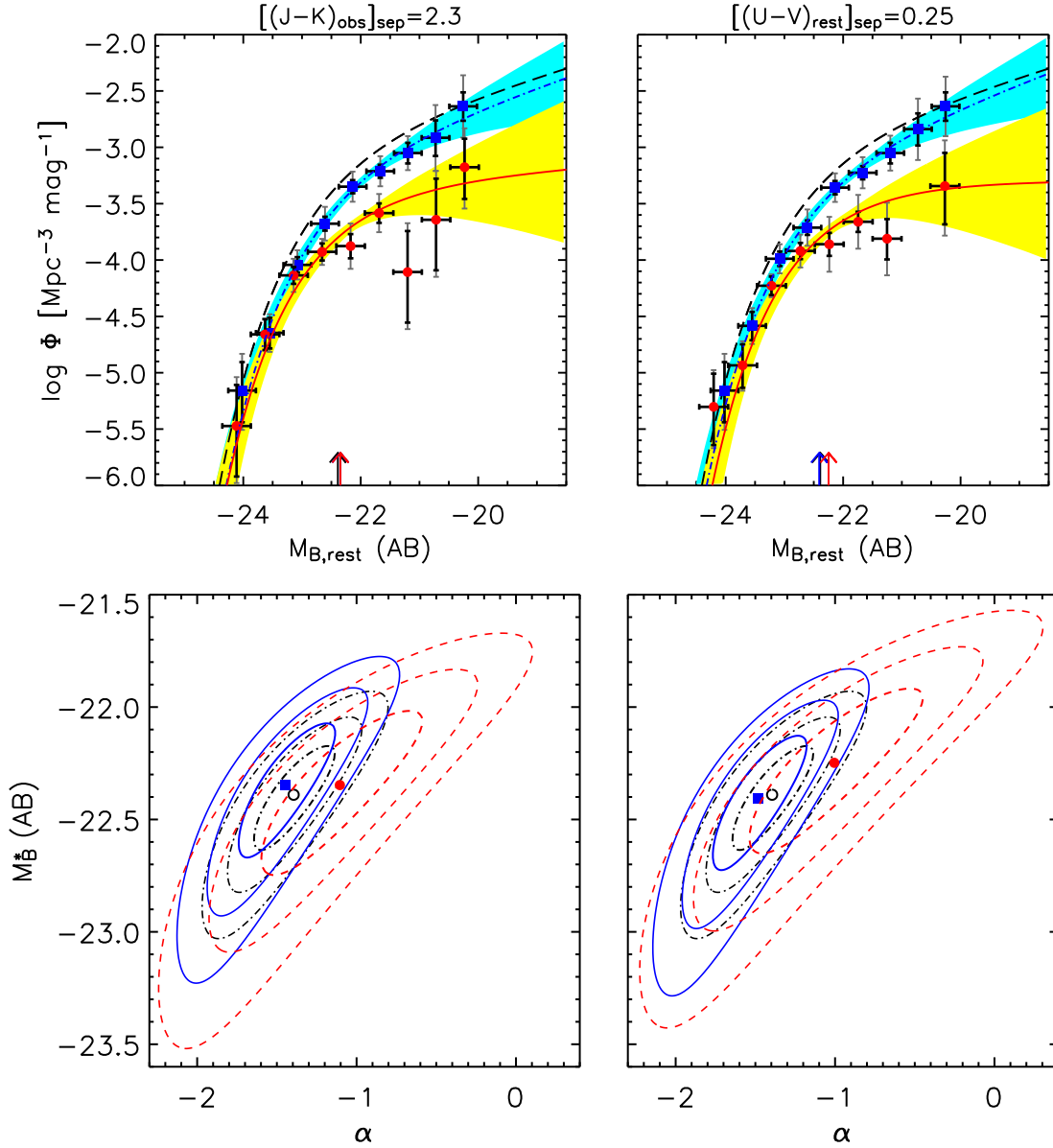


FIG. B3.— Rest-frame B-band LF at $2.5 < z \leq 3.5$; symbols as in Fig. B1.

The total area of their sample is $\sim 40 \text{ arcmin}^2$ over a single field, a factor of ~ 9.5 smaller than the total area sampled in this work.

A direct comparison between the B -band LF from Gabasch et al. (2004) and ours is possible in the redshift range $2.5 < z \leq 3.5$, and it is shown in the left panel of Figure C1 (*red symbols*). The best-fit Schechter parameters α , M^* , and Φ^* are consistent with ours within the errors. In the redshift range $2 \leq z \leq 2.5$ we compared our estimated B -band LF with the one defined by their best-fit Schechter parameters (α , M^* , and Φ^*) estimated at $z \sim 2.25$. While their best-fit Schechter parameters α and M^* are consistent with ours, their best-fit Φ^* is a factor of ~ 1.3 larger. This difference can be entirely accounted for by field-to-field variations (see § 5.1). In fact, the FDF survey consists of a single pointing of only $\sim 40 \text{ arcmin}^2$ and thus it is potentially strongly affected by sample variance. Moreover, Gabasch et al. (2004) spectroscopically identified an overdensity of galaxies at $z = 2.35$ (possibly a [proto]cluster, with more than 10 identical redshifts), which can potentially strongly bias the estimate of Φ^* in this redshift bin.

In the right panel of Figure C1 we compare our measured R -band LF with that measured by Gabasch et al. (2006) in the redshift range $1.91 < z < 2.61$. The agreement between the two LFs is much worse than for the rest-frame B -band. Their best-fit Schechter parameters α and M^* are now consistent with ours only at the $\sim 2 \sigma$ level, with their M^* about 0.3 mag brighter than ours; their best-fit Φ^* is a factor of ~ 1.6 larger than our best-fit value. As mentioned above, an overdensity of galaxies was spectroscopically found in this redshift interval in the FDF. Although it is hard to quantify the effect of the presence of a (proto)cluster at this redshift on the measured LF, it is interesting to make a connection with the work of Steidel et al. (2005), who spectroscopically identified a protocluster at $z = 2.3$ in the HS 1700+643 field. In the spectroscopically identified galaxy sample, Steidel et al. (2005) found 19 (out of 55) objects at $z = 2.300 \pm 0.015$ in the redshift range $2 < z < 2.5$. Within the $\sim 7' \times 7'$ field of view (similar to the FDF field of view) over which the protocluster objects are distributed, the protocluster and “field” galaxy

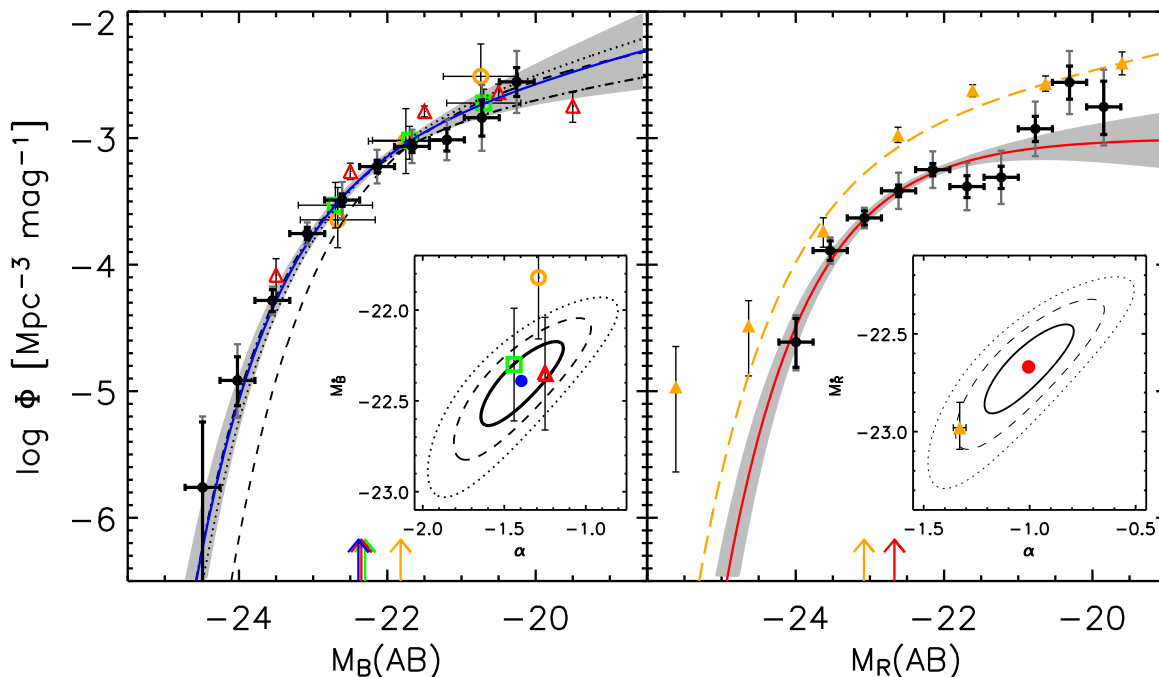


FIG. C1.— *Left*: Rest-frame B -band LF at $2.5 < z \leq 3.5$ from this work (blue solid line and black filled circles) compared to the LF from Poli et al. (2003; dotted line and green open squares), from Giallongo et al. (2005; dashed line and orange open circles), and from Gabasch et al. (2004; dot-dashed line and red open triangles). In the inset, the 1, 2, and 3 σ contour levels of the best-fit Schechter parameters α and M^* are compared to the best-fit values estimated by Poli et al. (2003), Giallongo et al. (2005), and Gabasch et al. (2004). *Right*: Rest-frame R -band LF at $2 \leq z \leq 2.5$ from this work (red solid line and black filled circles) compared to the LF from Gabasch et al. (2006; orange dashed line and filled triangles; $R = r - 0.12$). In the inset, the 1, 2, and 3 σ contour levels of the best-fit Schechter parameters α and M^* are compared to the best-fit values estimated by Gabasch et al. (2006).

sky distributions are the same. Assuming that the distribution of the spectroscopically identified galaxies is representative of the whole sample, the estimated density would be a factor of ~ 1.3 - 1.6 that of “field” galaxies only, consistent with the difference found in Φ^* between our composite sample and the FDF in the redshift range $2 < z < 2.5$.

C3. COMPARISON WITH GIALLONGO ET AL. (2005) FOR RED/BLUE GALAXIES

Giallongo et al. (2005) measured the rest-frame B -band LF of red and blue galaxies at redshift $2.5 < z < 3.5$ using a sample of 138 K -selected galaxies in the redshift range $1.3 < z < 3.5$ down to $K_{AB} = 25$. Their red and blue populations were defined on the basis of an “S0 color track”. From their Figure 1, the average rest-frame $U - V$ color of their model at redshift $2.5 < z < 3.5$ is ~ 0.22 , very similar to our definition of blue and red galaxies ($U - V < 0.25$ and $U - V \geq 0.25$, respectively). In Figure C2 we have compared the LFs of red and blue galaxies from this work to those presented in Giallongo et al. (2005).

As for the LF of all galaxies, we are able to constrain the bright end of the LF much better by sampling the LF to luminosities ~ 1.5 mag brighter. For the red galaxy population, their measurements of the LF with the $1/V_{\max}$ method are consistent within the errors with ours; their best-fit faint-end slope is also consistent, within the errors, with our estimate, although α was fixed at the local value in Giallongo et al. (2005); our M^* is ~ 0.4 mag brighter than their best-fit value, but still consistent within the errors at the 1σ level. The best-fit normalization of Giallongo et al. (2005) is a factor of ~ 1.5 smaller than ours, only marginally consistent at the 2σ level.

For the blue population, the $1/V_{\max}$ measurements of the LF from Giallongo et al. (2005) are consistent with ours. However, the agreement gets worse when we compare our LF estimated using the STY method with theirs, especially at the bright end, where they lack information. While their assumed faint-end slope is consistent with our best-fit solution, the characteristic magnitude from Giallongo et al. (2005) is ~ 0.7 mag fainter than ours. Their best-fit solution is, however, very uncertain, characterized by very large error bars and still consistent with ours at the $\sim 1 \sigma$ level.

REFERENCES

- Adelberger, K. L., Erb, D. K., Steidel, C. C., Reddy, N. A., Pettini, M., & Shapley, A. E. 2005, *ApJ*, 620, L75
 Adelberger, K. L., & Steidel, C. C. 2000, *ApJ*, 544, 218
 Adelberger, K. L., Steidel, C. C., Shapley, A. E., Hunt, M. P., Erb, D. K., Reddy, N. A., & Pettini, M. 2004, *ApJ*, 607, 226
 Avni, Y. 1976, *ApJ*, 210, 642
 Avni, Y., & Bahcall, J. N. 1980, *ApJ*, 235, 694
 Bell, E. F., de Jong, R. S. 2001, *ApJ*, 550, 212
 Bessell, M. S. 1990, *PASP*, 102, 1181
 Blanton, M. R., et al. 2001, *AJ*, 121, 2358
 Blanton, M. R., et al. 2003, *ApJ*, 592, 819
 Brown, W. R., Geller, M. J., Fabricant, D. G., Kurtz, M. J. 2001, *AJ*, 2001, 122, 714
 Bruzual, G., & Charlot, S. 2003, *MNRAS*, 344, 1000
 Calzetti, D., Armus, L., Bohlin, R. C., Kinney, A. L., Koornneef, J., & Storchi-Bergmann, T. 2000, *ApJ*, 533, 682
 Chabrier, G. 2003, *PASP*, 115, 763
 Chen, H.-W., et al. 2003, *ApJ*, 586, 745
 Cole, S., et al. 2001, *MNRAS*, 326, 255
 Coleman, G. D., Wu, C.-C., Weedman, D. W. 1980, *ApJS*, 43, 393
 Daddi, E., et al. 2003, *ApJ*, 588, 50
 Dahlen, T., Mobasher, B., Somerville, R. S., Moustakas, L. A., Dickinson, M., Ferguson, H. C., Giavalisco, M. 2005, *ApJ*, 631, 126
 Davis, M., et al. 2003, *Proc. SPIE*, 4834, 161
 Efstathiou, G., Ellis R. S., & Peterson, B. A. 1988, *MNRAS*, 232, 431

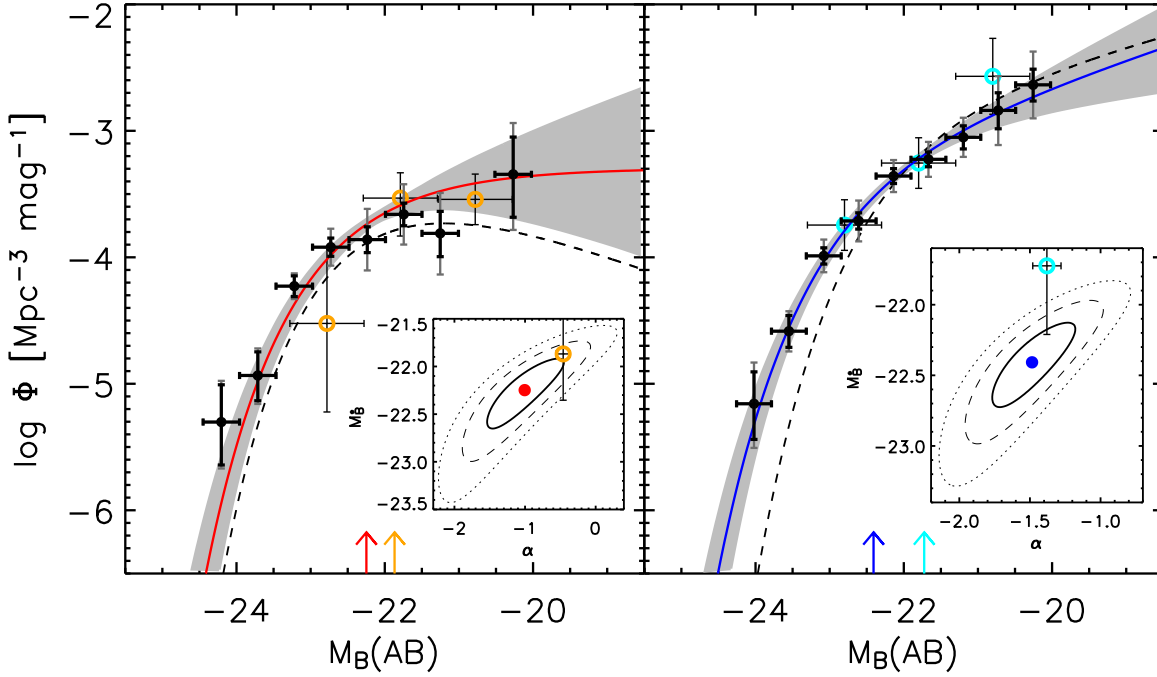


FIG. C2.— *Left*: Rest-frame B -band LF at $2.5 < z \leq 3.5$ from this work for red galaxies ($U - V \geq 0.25$; red solid line and black filled circles) compared to the one from Giallongo et al. (2005; dashed line and orange open circles); in the inset, the 1, 2, and 3 σ contour levels of the best-fit Schechter parameters α and M^* are compared to the best-fit values estimated by Giallongo et al. (2005; orange open circle), which assumed a constant $\alpha = -0.46$. *Right*: Rest-frame B -band LF at $2.5 < z \leq 3.5$ from this work for blue galaxies ($U - V < 0.25$; blue solid line and black filled circles) compared to the one from Giallongo et al. (2005; dashed line and cyan open circles); in the inset, the 1, 2, and 3 σ contour levels of the best-fit Schechter parameters α and M^* are compared to the best-fit values estimated by Giallongo et al. (2005; cyan open circle), which assumed a constant $\alpha = -1.38$.

- Ellis R. S., Colless, M., Broadhurst, T., Heyl, J., Glazebrook, K. 1996, MNRAS, 280, 235
- Förster Schreiber, N. M., et al. 2004, ApJ, 616, 40
- Förster Schreiber, N. M., et al. 2006, AJ, 131, 1891
- Franx, M., et al. 2003, ApJ, 587, L79
- Gabasch, A., et al. 2004, A&A, 421, 41
- Gabasch, A., et al. 2006, A&A, 448, 101
- Gawiser, E., et al. 2006, ApJS, 162, 1
- Gehrels, N. 1986, ApJ, 303, 336
- Giallongo, E., Salimbeni, S., Menci, N., Zamorani, G., Fontana, A., Dickinson, M., Cristiani, S., Pozzetti, L. 2005, ApJ, 622, 116
- Giavalisco, M., et al. 2004, ApJ, 600, L93
- Hauschildt, P. H., Allard, F., & Baron, E. 1999, ApJ, 512, 377
- Heidt, J., et al. 2003, A&A, 398, 49
- Ilbert, O., et al. 2005, A&A, 439, 86
- Kauffmann, G., et al. 2003, MNRAS, 341, 33
- Kendall, M. G., & Stuart, A. 1961, The Advanced Theory of Statistics, Vol. 2 (London: Griffin & Griffin)
- Kinney, A. L., Calzetti, D., Bohlin, R. C., McQuade, K., Storchi-Bergmann, T., & Schmitt, H. R. 1996, ApJ, 467, 38
- Knudsen, K. K., et al. 2005, ApJ, 632, L9
- Kochanek, C. S., et al. 2001, ApJ, 560, 566
- Kriek, M. et al. 2006, ApJ, 649, L71
- Labbé, I., et al. 2003, AJ, 125, 1107
- Labbé, I., et al. 2005, ApJ, 624, L81
- Labbé, I., et al. 2006, ApJ, submitted
- Lampton, M., Margon, B., & Bowyer, S. 1976, ApJ, 208, 177
- Le Fèvre, et al. 2004, A&A, 417, 839
- Lilly, S.J., Tresse, L., Hammer, F., Crampton, D., Le Fèvre, O. 1995, ApJ, 455, 108
- Lin, H., Yee, H. K. C., Carlberg, R. G., Ellingson, E. 1997, ApJ, 475, 494
- Nagamine, K., Cen, R., & Ostriker, J. P. 2000, ApJ, 541, 25
- Nagamine, K., Fukugita, M., Cen, R., & Ostriker, J. P. 2001, MNRAS, 327, L10
- Norberg, P., et al. 2002, MNRAS, 336, 907
- Papovich, C., et al. 2006, ApJ, 640, 92
- Pettini, M., Shapley, A. E., Steidel, C. C., Cuby, J.-G., Dickinson, M., Moorwood, A. F. M., Adelberger, K. L., & Giavalisco, M. 2001, ApJ, 554, 981
- Poli, F., et al. 2003, ApJ, 593, L1
- Quadri, R., et al. 2007a, ApJ, 654, 138
- Quadri, R., et al. 2007b, AJ, submitted (astro-ph/0612612)
- Reddy, N. A., Erb, D. K., Steidel, C. C., Shapley, A. E., Adelberger, K. L., Pettini, M. 2005, ApJ, 633, 748
- Reddy, N. A., Steidel, C. C., Fadda, D., Yan, L., Pettini, M., Shapley, A. E., Erb, D. K., Adelberger, K. L. 2006, ApJ, 644, 792
- Rubin, K. H. R., van Dokkum, P. G., Coppi, P., Johnson, O., Förster Schreiber, N. M., Franx, M., & van der Werf, P. 2004, ApJ, 613, L5
- Rudnick, G., et al. 2001, AJ, 122, 2205
- Rudnick, G., et al. 2003, ApJ, 599, 847
- Rudnick, G., et al. 2006, ApJ, 650, 624
- Salpeter, E. E. 1955, ApJ, 121, 161
- Sandage, A., Tammann, G. A., & Yahil, A. 1979, ApJ, 232, 352
- Saracco, P., Giallongo, E., Cristiani, S., D'Odorico, S., Fontana, A., Iovino, A., Poli, F., & Vanzella, E. 2001, A&A, 375, 1
- Sawicki, M., & Thompson, D. 2005, ApJ, 635, 100
- Sawicki, M., & Thompson, D. 2006, ApJ, 642, 653
- Schechter, P. 1976, ApJ, 203, 297
- Schmidt, M. 1968, ApJ, 151, 393
- Shapley, A. E., Erb, D. K., Pettini, M., Steidel, C. C., & Adelberger, K. L. 2004, ApJ, 612, 108
- Shapley, A. E., Steidel, C. C., Adelberger, K. L., Dickinson, M., Giavalisco, M., & Pettini, M. 2001, ApJ, 562, 95
- Shapley, A. E., Steidel, C. C., Erb, D. K., Reddy, N. A., Adelberger, K. L., Pettini, M., Barmby, P., & Huang, J. 2005, ApJ, 626, 698
- Steidel, C. C., Adelberger, K. L., Giavalisco, M., Dickinson, M., & Pettini, M. 1999, ApJ, 519, 1
- Steidel, C. C., Adelberger, K. L., Shapley, A. E., Erb, D. K., Reddy, N. A., & Pettini, M. 2005, ApJ, 626, L44
- Steidel, C. C., Adelberger, K. L., Shapley, A. E., Pettini, M., Dickinson, M., & Giavalisco, M. 2003, ApJ, 592, 728
- Steidel, C. C., Giavalisco, M., Pettini, M., Dickinson, M., & Adelberger, K. L. 1996, ApJ, 462, L17
- Steidel, C. C., Shapley, A. E., Pettini, M., Adelberger, K. L., Erb, D. K., Reddy, N. A., & Hunt, M. P. 2004, ApJ, 604, 534
- van Dokkum, P. G., et al. 2003, ApJ, 587, L83
- van Dokkum, P. G., et al. 2004, ApJ, 611, 703
- van Dokkum, P. G., et al. 2006, ApJ, 638, 59
- Wolf, C., Meisenheimer, K., Rix, H.-W., Borch, A., Dye, S., Kleinheinrich, M. 2003, A&A, 401, 73
- Zucca, E., et al. 2006, A&A, 445, 879